Monthly Notices
of the
ROYAL ASTRONOMICAL SOCIETY

MNRAS **466,** 425–442 (2017)
Advance Access publication 2016 October 8

doi:10.1093/mnras/stw2577

Optimal scan strategies for future CMB satellite experiments

Christopher G. R. Wallis,[1,2]★ Michael L. Brown,[1] Richard A. Battye[1] and Jacques Delabrouille[3]

[1]*Jodrell Bank Centre for Astrophysics, School of Physics and Astronomy, The University of Manchester, Oxford Road, Manchester M13 9PL, UK*
[2]*Mullard Space Science Laboratory, University College London, Surrey RH5 6NT, UK*
[3]*APC, 10, rue Alice Domon et Leonie Duquet, F-75205 Paris Cedex 13, France*

Accepted 2016 October 7. Received 2016 October 5; in original form 2016 April 8; Editorial Decision 2016 October 5

ABSTRACT

The B-mode polarization power spectrum in the cosmic microwave background (CMB) is about four orders of magnitude fainter than the CMB temperature power spectrum. Any instrumental imperfections that couple temperature fluctuations to B-mode polarization must therefore be carefully controlled and/or removed. We investigate the role that a scan strategy can have in mitigating certain common systematics by averaging systematic errors down with many crossing angles. We present approximate analytic forms for the error on the recovered B-mode power spectrum that would result from differential gain, differential pointing and differential ellipticity for the case where two detector pairs are used in a polarization experiment. We use these analytic predictions to search the parameter space of common satellite scan strategies in order to identify those features of a scan strategy that have most impact in mitigating systematic effects. As an example, we go on to identify a scan strategy suitable for the CMB satellite proposed for the European Space Agency M5 call, considering the practical considerations of fuel requirement, data rate and the relative orientation of the telescope to the earth. Having chosen a scan strategy we then go on to investigate the suitability of the scan strategy.

Key words: methods: observational – cosmic background radiation – cosmology: observations – inflation.

1 INTRODUCTION

The cosmic microwave background (CMB) B-mode polarization represents a powerful cosmological probe. In particular, certain early Universe models predict large-scale B-mode polarization due to gravitational waves created during inflation. On smaller scales gravitational lensing of the stronger E-mode polarization creates a lensing B-mode polarization signal. Observationally, a great deal of effort has been devoted in recent times to measuring the B-mode polarization signal. The Keck/BICEP2 series of experiments (Keck Array and BICEP2 Collaborations et al. 2015) have produced the deepest polarization maps at 95 and 150 GHz, thus providing tight constraints on the amplitude of the large-scale ($\ell \lesssim 100$) B-mode polarization power spectrum. This constraint was only made possible due to the wide frequency range of polarization maps provided by the *WMAP* and *Planck* experiments (Bennett et al. 2013; Planck Collaboration I 2016) – the low-frequency maps constrain the foreground synchrotron emission and the high-frequency maps constrain the level of foreground polarized dust emission. The smaller scale ($\ell \approx 500$–2000) lensing B-mode signal has been detected by a number of groups thus providing constraints on large-scale structures (The Polarbear Collaboration: P. A. R. Ade et al. 2014; Hanson et al. 2013).

The B-mode polarization power spectrum is approximately four orders of magnitude smaller than the temperature power spectrum. Therefore, any coupling between the two must be carefully controlled and/or removed. Previous analytic work on this topic has focused on predicting the levels of leakage (Hu, Hedman & Zaldarriaga 2003; O'Dea, Challinor & Johnson 2007; Shimon et al. 2008; Wallis et al. 2014), while experimental teams have included a careful assessment of its impact. For example, the Polarbear Collaboration addressed the issue of temperature to polarization leakage with detailed simulations (The Polarbear Collaboration: P. A. R. Ade et al. 2014). Using these, they showed that the leakage was significantly below the B-mode polarization power spectrum signal that they had detected. The Planck Low Frequency Instrument examined temperature to polarization leakage extensively pre-launch (Leahy et al. 2010). The BICEP2 team found levels of temperature leakage that were a factor of a few above the B-mode polarization power spectrum signal. They therefore developed and applied techniques to remove the leakage by fitting for it in the polarization timestream (BICEP2 Collaboration et al. 2015). In addition to removing the temperature leakage, this approach removes genuine polarization signal that must be accounted for in the subsequent estimation of polarization power spectra. It would therefore be beneficial to

★ E-mail: chris.wallis@ucl.ac.uk

either use techniques that do not require such fitting (e.g. Wallis et al. 2015) or, preferably, to design an experiment sufficiently well such that the leakage is insignificant.

Here, we examine how satellite scan strategies can be designed to mitigate various systematic effects that couple temperature to polarization for satellite-based experiments. In our study, we focus on differencing experiments, consisting of pairs of detectors. Within each pair, one detector is sensitive to the CMB temperature and polarization signal in a particular direction on the sky, convolved with some detector response function. The other detector is, in principle, sensitive to the same temperature signal but has a polarization sensitivity that is rotated by 90°. By differencing the timestreams of these two detectors, the temperature response is removed. However, any differences between the two temperature response functions of the detectors will couple temperature fluctuations to the polarization map.

In this study, we consider three types of mismatch between the two temperature response functions, all of which were found to be present in the BICEP2 experiment (BICEP2 Collaboration et al. 2015). First, we consider a difference in the gain calibration of the two detectors which we term 'differential gain'. We note that differential gain can couple the CMB dipole to the polarization maps. Here we ignore this contribution since it will only affect the lowest multipoles. We also note that a difference in the spectral windows of the two detectors, as has been shown to exist, for instance, in Planck bolometer pairs (Planck Collaboration VII 2016), is equivalent to a 'differential' gain effect that depends on the emission law, and thus is different for different astrophysical components. We further note that such a 'bandpass mismatch' will result in temperature to polarization leakage of foreground signals even in the case where the detectors are perfectly calibrated. We also consider a difference in the pointing direction of the two detector response functions, which we call 'differential pointing'. Finally, we investigate the impact of a 'differential ellipticity' arising from a difference in the beam ellipticities of the two detectors.

The systematics that we consider are typical for the type of experimental setup that we have chosen. By using bolometers, which do not conserve the phase of the incoming radiation, either detector differencing or polarization angle rotation must be used to disentangle the polarization signal from the temperature response of the detector. Modern bolometers are close to photon noise limited and are therefore preferred by state-of-the-art CMB polarization experiments. The South Pole Telescope (Padin et al. 2008), BICEP2 (BICEP2 Collaboration et al. 2014) and the Polarbear Collaboration (The Polarbear Collaboration: P. A. R. Ade et al. 2014) all use bolometers. Using a half-wave plate (HWP) can allow one to make maps of temperature and polarization without differencing. If the HWP is continually rotating, then certain 'lock-in' techniques can be used to isolate the polarization signal from the systematic errors (Wu et al. 2007). However, maintaining continuous rotation of the HWP can cause its own wealth of systematic errors. A stepped HWP can also be used to increase the polarization angle coverage but it is less effective than a rotating HWP in terms of mitigating systematic effects (Brown et al. 2009). However, systematic effects associated with the HWP itself are much easier to control when the HWP is stepped.

Previous work has been undertaken to identify optimal scan strategies for CMB satellite experiments. Delabrouille et al. (2000) identified the requirements for the scan strategy for the *Planck* mission. One of these requirements was the need to have multiple crossing angles in order to mitigate systematic errors that depend on the orientation, or parallactic angle, of the telescope – a problem that we also consider in this paper. Delabrouille, Gorski & Hivon (1998) looked at the increase of noise due to instrumental drift, or $1/f$ noise, and the benefit that a well-chosen scan strategy can have on the final power spectrum analysis. The benefits of different scan strategies for *Planck* were also investigated in Dupac & Tauber (2005), where the authors attempt to maximize the uniformity of the integration time over the sky.

The aim of our study is to examine the degree to which a scan strategy can mitigate systematic errors by averaging their effects through multiple observations of the same sky pixel with different instrument orientations. To do this, we first derive a set of simple equations that predict the error on the recovered B-mode polarization power spectrum given a few characteristics of the scan strategy and the amplitude of the systematic effect. We then go on to use these simple equations to predict the error on the B-mode polarization power spectrum for different satellite scan strategies. This allows us to clearly identify those features of a scan strategy that have the most impact in controlling the level of instrumental B-mode polarization.

There are a number of major proposed CMB polarization satellite missions for which our work is relevant. A proposal for a CMB polarization satellite is currently being prepared for submission to the European Space Agency (ESA)'s recently announced 'M5' call for proposals for a medium-sized mission. This proposal – which we loosely refer to hereafter as 'COrE++' – builds on the previous COrE[1] (The COrE Collaboration et al. 2011) and COrE+ proposals that were submitted to ESA's previous M3 and M4 calls, respectively. The primary science goal of COrE++ will be to constrain the inflationary B-mode polarization signal to a precision of $\sigma_r \sim 10^{-3}$ (where r is the tensor-to-scalar ratio). However, the COrE++ concept will also facilitate many other science goals including precision CMB lensing measurements and Sunyaev–Zel'dovich cluster counts. The Japan Aerospace Exploration Agency has a well-developed proposal named 'Lite (Light) satellite for the studies of B-mode polarization and Inflation from cosmic background Radiation Detection' (LiteBIRD; Matsumura et al. 2014). The LiteBIRD team has built many features into the design of the experiment to mitigate systematic effects, including an HWP providing the experiment with additional polarization angle modulation. Another proposed mission is the Primordial Inflation Explorer (PIXIE; Kogut et al. 2011), which also focuses on inflationary B modes as its primary science goal. The PIXIE concept makes use of a polarizing Fourier transform spectrometer to measure both the linear polarization and the spectral dependence of the microwave sky over a large range of frequencies, from 30 GHz to 6 THz. In this paper, we have particularly focused on the scan-strategy options for the COrE++ mission concept. However, our results are, in general, enough that they should also be useful for the design of scan strategies for other such satellite missions.

The paper is organized as follows. In Section 2, we derive the equations that predict the temperature-to-polarization leakage due to three main systematic effects that are of concern for CMB polarization measurements. In Section 3, we use time-order data (TOD) simulations to demonstrate the validity of the equations derived in Section 2. In Section 4, we search the main parameter space of satellite scan strategies to identify those key features that have the largest impact in terms of mitigating systematic effects. In Section 5, we demonstrate how the tools developed in the previous sections can

[1] See www.core-mission.org

be used to identify an 'optimal' scan strategy for COrE++. Finally, in Section 6 we summarize our results.

2 IMPACT OF SYSTEMATICS ON THE B-MODE POWER SPECTRUM

To assess the impact of the systematic effects on the recovered B-mode power spectrum, we begin by considering the detected signal from a single pair of detectors.

We describe the pointing of the telescope using Euler angles, $\boldsymbol{\omega} = (\theta, \phi, \psi)$. The Euler angles represent a sequence of three active rotations (starting from some fiducial initial orientation). They are active in the sense that the beam moves with respect to the coordinate system. The following series of steps describe how to rotate the beam from the fiducial orientation to the orientation described by $\boldsymbol{\omega}$, all rotations being performed clockwise when looking along the axis in the positive direction, that is they are performed in a right-handed sense.

(i) The beam is rotated around the z-axis by ψ.
(ii) The beam is rotated by θ around the y-axis.
(iii) The beam is rotated around the z-axis again by ϕ.

The detected signal from a single detector pointing at sky position $\boldsymbol{\omega}$ is

$$d_i^X = \int \mathrm{d}\Omega [B^T_{X\boldsymbol{\omega}}(\Omega) T(\Omega) + B^Q_{X\boldsymbol{\omega}}(\Omega) Q(\Omega) + B^U_{X\boldsymbol{\omega}}(\Omega) U(\Omega)], \quad (1)$$

where i denotes the pair that the detector belongs to; Ω describes the angle on the sphere; and $X = \{a, b\}$ distinguishes between the two detectors within a pair. $B^Y_{X\boldsymbol{\omega}}(\Omega)$ is the beam response function of detector X to the Stokes parameters $Y = \{T, Q, U\}$ when pointing at sky position $\boldsymbol{\omega}$. In this work, we focus on the most problematic systematic effects for CMB B-mode experiments – those which couple the temperature signal to polarization maps. We consider a differencing experiment, i.e. one where each instrument 'pixel' is composed of two detectors which are sensitive to orthogonal polarization directions. The timestream from the two detectors in a pair can be summed to obtain the temperature of the sky and differenced to obtain a measurement of the polarization. Therefore, any mismatch in the response of the two detectors to the temperature sky will result in this type of leakage. Note that we ignore all leakage effects between polarization Stokes parameters (Q, U) as any such effects will be subdominant compared to the leakage from temperature. Explicitly the differenced signal is

$$d_i = \frac{1}{2}\left(d_i^a - d_i^b\right). \quad (2)$$

One important characteristic of a systematic error when considering the impact on the recovered polarization maps and power spectra is the spin of the systematic error. The spin is defined by how the temperature leakage rotates with the orientation of the telescope for a particular sky pixel. Here we have defined the orientation angle by ψ, which is the angle between the orientation of the focal plane and the direction to the north pole. This is often referred to as the parallactic angle of the telescope. If the systematic error is of a different spin to the spin-2 polarization signal, and if a sky pixel is observed at many instrument orientations, then the resulting bias on the measured polarization is reduced. The primary goal of this study is to examine the effectiveness of different scan strategies to mitigate systematic errors in this way. To facilitate this, we derive a set of simple analytic equations to model the leaked B-mode polarization power spectrum. The first stage of the derivation is to calculate the leakage of the temperature signal into the polarization timestream for each systematic error.

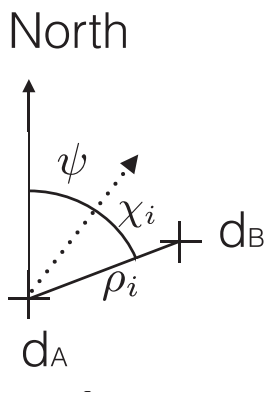

Figure 1. Schematic diagram showing the parameters used to define the differential pointing of a detector pair, viewed from inside the sphere. The detector beams are centred at an angle ρ_i with respect to each other, in a direction which is an angle χ_i with respect to the scan direction, which in turn is an angle ψ from north.

2.1 Leakage in the differenced timestream

We start by examining the effect of differential gain on the differenced signal from a detector pair. This is simply a miscalibration between the two detectors of δg_i. The temperature leakage, δd_i^{g}, due to differential gain (δg_i) in detector pair i is

$$\delta d_i^{\mathrm{g}} = \frac{1}{2}(T^{\mathrm{B}}(\Omega) - (1 - \delta g_i) T^{\mathrm{B}}(\Omega)) \quad (3)$$

$$= \frac{1}{2}\delta g_i T^{\mathrm{B}}(\Omega), \quad (4)$$

$$= G^i \quad (5)$$

where $T^{\mathrm{B}}(\Omega)$ denotes the CMB temperature sky convolved with the axisymmetric part of the temperature beam and this defines the level of the systematic gain, G^i. This systematic effect is independent of the orientation of the telescope with respect to the sky coordinates. It depends only on the size of the temperature signal in the direction in which the telescope is pointing at any given time. Differential gain is, therefore, a spin-0 systematic effect.

The second systematic effect we consider is differential pointing. This is a misalignment of the two detector beams by some angle ρ_i in a direction χ_i with respect to the orientation of the telescope from north (ψ), see Fig. 1 . As the differential pointing will be a small angle, we make the flat sky approximation. We consider a Cartesian coordinate system where the y-axis is aligned with north. The error in the differenced timestream can then be modelled as

$$\delta d_i^{\mathrm{p}} = \frac{1}{2}[T^{\mathrm{B}}(x, y) - T^{\mathrm{B}}(x - \rho_i \sin(\psi + \chi_i), y - \rho_i \cos(\psi + \chi_i))]. \quad (6)$$

If we Taylor expand around (x, y) to first order in ρ_i, we find

$$\delta d_i^{\mathrm{p}} = \frac{1}{2}\left[\frac{\partial T^{\mathrm{B}}}{\partial x}\rho_i \sin(\psi + \chi_i) + \frac{\partial T^{\mathrm{B}}}{\partial y}\rho_i \cos(\psi + \chi_i)\right], \quad (7)$$

$$= \frac{1}{4}\left[\left(\frac{\partial T^{\mathrm{B}}}{\partial y} - \mathrm{i}\frac{\partial T^{\mathrm{B}}}{\partial x}\right)\rho_i \mathrm{e}^{\mathrm{i}(\psi + \chi_i)} + \mathrm{c.c.}\right], \quad (8)$$

$$= \frac{1}{2}(M^i \mathrm{e}^{\mathrm{i}\psi} + \mathrm{c.c.}) \quad (9)$$

where c.c. denotes the complex conjugate of the first term inside the square bracket and this defines the systematic due to differential pointing M^i. The $e^{i\psi}$ term signifies the known result that differential pointing is a spin-1 systematic effect.

The final systematic effect we consider is a differential ellipticity between the detector pairs. To treat this, it is convenient to write the integration in equation (1) in spherical harmonic space. For simplicity, we use a coordinate system with the north pole coincident with the pointing centre. We denote the beam decomposed into spherical harmonics as $b^X_{\ell k}$ and the temperature sky is denoted by $a^T_{\ell m}$. The error on the differenced signal between the two detectors within a pair is then

$$\delta d^{\rm e}_i = \frac{1}{2}\sum_{\ell m}\sqrt{\frac{4\pi}{2\ell+1}}\left(b^a_{\ell m}a^{T*}_{\ell m} - b^b_{\ell m}a^{T*}_{\ell m}\right), \tag{10}$$

$$\approx \frac{1}{2}\sum_{\ell}\sqrt{\frac{4\pi}{2\ell+1}}\left(\delta b^i_{\ell,2}a^{T*}_{\ell,2} + \delta b^i_{\ell,-2}a^{T*}_{\ell,-2}\right), \tag{11}$$

where we have assumed that the axisymmetric components of the two detector beams cancel and that the dominant remaining term is the second azimuthal mode.This is demonstrated to be true for an elliptical Gaussian beam in fig. 2 of Wallis et al. (2014). When the telescope orientation is changed, but the same patch of sky is observed, this differential ellipticity will rotate as, $\delta b'_{\ell,2} = e^{i2\psi}\delta b_{\ell,2}$. This rotation makes the differential ellipticity effect a spin-2 effect. We can, therefore, rewrite the temperature leakage due to differential ellipticity as a function of the orientation of the telescope as

$$\delta d^{\rm e}_i \approx \frac{1}{2}\sum_{\ell}\sqrt{\frac{4\pi}{2\ell+1}}(\delta b^i_{\ell,2}a^{T*}_{\ell,2}e^{i2\psi} + \delta b^i_{\ell,-2}a^{T*}_{\ell,-2}e^{-i2\psi}), \tag{12}$$

$$= \frac{1}{2}(E^i e^{i2\psi} + \text{c.c.}), \tag{13}$$

which defines E^i.

2.2 Temperature leakage to the polarization map

We can combine the above understanding of the temperature leakage effects due to the various systematics to create a model for the differenced signal as a function of the orientation of the telescope. The differenced signal from a detector pair i for a single sky pixel is given by

$$S^i(\psi) = G^i + \frac{1}{2}[Pe^{i2\psi} + M^i e^{i\psi} + E^i e^{i2\psi} + \text{c.c.}], \tag{14}$$

where $P = Q + iU$ is the complex representation of the polarization signal in the sky pixel. G^i, M^i and E^i are the contributions to the differenced signal from the three systematic effects we are considering – differential gain, pointing and ellipticity, respectively. The exact forms of G^i, M^i and E^i are defined in equations (5), (9) and (13). To understand the effect that these systematics have on the recovered power spectrum, we first examine the effect that they have on the map.

In general, each pixel of a map will be observed at a variety of orientation angles ψ. We define the detected signal as S^d which is the information that we have about the pixel as a function of the orientation:

$$S^d(\psi) = h(\psi)S(\psi), \text{ where} \tag{15}$$

$$h(\psi) = \frac{2\pi}{N_{\rm hits}}\sum_j \delta(\psi - \psi_j). \tag{16}$$

Here, ψ_j is the orientation of the jth observation (or 'hit') of the pixel and the sum is over all such observations, $N_{\rm hits}$.

Let us now consider the signal seen by two detector pairs. To do this, imagine an 'instrument-Q' detector pair whose orientation with respect to the sky coordinates for the jth observation is labelled as ψ_j and an 'instrument-U' pair of detectors whose polarization sensitivity directions are rotated by $\pi/4$ with respect to those of the 'instrument-Q' detectors. For every hit, there will then be two orientations, one at ψ_j and the other at $\psi_j + \pi/4$, each with different systematic effects. We can therefore write

$$S^d_{\rm tot}(\psi) = h(\psi)S^1(\psi) + h(\psi - \pi/4)S^2(\psi), \tag{17}$$

which we can write in Fourier space as a convolution:[2]

$$\tilde{S}^d_k = \sum_{k'=-\infty}^{\infty}\tilde{h}_{k-k'}\tilde{S}^1_{k'} + \tilde{h}_{k-k'}e^{i\pi(k'-k)/4}\tilde{S}^2_{k'}. \tag{18}$$

From equation (14), we can see that $S^i(\psi)$ is made up of only a few Fourier terms. Therefore, equation (18) can also be limited to just a few terms, explicitly the $k' = -2$ to $k' = 2$ terms. We can use these simplifications to write out the $k = 2$ row of $\tilde{S}^d_k$:

$$\tilde{S}^d_2 = \tilde{h}_0\left(\tilde{S}^1_2 + \tilde{S}^2_2\right) + \tilde{h}_1\left(\tilde{S}^1_1 + e^{i\pi/4}\tilde{S}^2_1\right) + \tilde{h}_2\left(\tilde{S}^1_0 + i\tilde{S}^2_0\right) + \tilde{h}_3\left(\tilde{S}^1_{-1} + e^{i3\pi/4}\tilde{S}^2_{-1}\right) + \tilde{h}_4\left(\tilde{S}^1_{-2} - \tilde{S}^2_{-2}\right). \tag{19}$$

We can see from the definition of $h(\psi)$ in equation (16) that $\tilde{h}_0 = 1$; also from equation (14) we can see that $S^i_2 = P/2$ and $S^i_{-2} = P^*/2$. Therefore, in the absence of any systematic effects or instrumental noise, $\tilde{S}^d_2 = P$. In a simple binning map-making scheme, this leads to an estimate of the polarization in a pixel. We can now deduce the spurious polarization signal by examining equation (19). Any additional terms, beyond the expected P, will be spurious. Performing this analysis for the systematic effects we have considered, and defining the differential operator $\nabla = (\partial/\partial y - i\partial/\partial x)$, we find the following systematic terms in the polarization maps:

$$\Delta P^{\rm g} = \frac{1}{2}\tilde{h}_2(\delta g_1 + i\delta g_2)T^{\rm B}, \tag{20}$$

$$\Delta P^{\rm p} = \frac{1}{4}\tilde{h}_1\nabla T^{\rm B}(\rho_1 e^{i\chi_1} + \rho_2 e^{i(\chi_2+\pi/4)}) + \frac{1}{4}\tilde{h}_3\nabla^* T^{\rm B}(\rho_1 e^{-i\chi_1} + \rho_2 e^{-i(\chi_2-3\pi/4)}), \tag{21}$$

$$\Delta P^{\rm e} = \frac{1}{2}\sqrt{\frac{4\pi}{2\ell+1}}(\delta b^1_{\ell,2} + \delta b^2_{\ell,2})a^{T*}_{\ell,2} + \frac{1}{2}\tilde{h}_4\sqrt{\frac{4\pi}{2\ell+1}}(\delta b^1_{\ell,-2} - \delta b^2_{\ell,-2})a^{T*}_{\ell,-2}. \tag{22}$$

2.3 Temperature leakage to the B-mode power spectrum

We now wish to calculate the error on the B-mode polarization power spectrum. As the window function, $h(\psi)$, will be different for each pixel, an exact calculation is a difficult computational task.

[2] The Fourier transform and inverse we use are

$$\tilde{f}_k = \frac{1}{2\pi}\int_0^{2\pi} d\psi e^{ik\psi} f(\psi),$$

$$f(\psi) = \sum_{k=-\infty}^{\infty}\tilde{f}_k e^{-ik\psi}.$$

Table 1. Description of the variables used in the analysis (see Sections 2 and 3 in the main text) and the values adopted for the simulations.

Symbol	Description	Value set to in relevant simulation
ψ	The orientation of the scan direction with respect to north	Varies with scan strategy, positionand time
$\tilde{h}_n$	The average of the complex exponential of the orientations for a pixel, $\langle\, \mathrm{e}^{in\psi}\rangle_{\rm hits}$	Varies with scan and pixel
FWHM	The full width at half the maximum of the beam	7 arcmin for all the simulations
δg_i	The differential gain between the two detectorsin pair i	0.01 for both detector pairs
ρ_i	The angle between the two beam centres in pair i	0.1 arcmin for both (1.5 per cent of the FWHM)
χ_i	The orientation of the second beam from the the first in a detector pair i relative to the direction of the scan	0 and $\pi/4$
$b_{\ell m}$	The spherical harmonic decomposition of the temperature beam	That of an elliptical Gaussian – see equation (29)
$\delta b^i_{\ell m}$	The spherical harmonic decomposition of the difference of the temperature beams of pair i	That of an elliptical Gaussian – see equation (29)
q	Ellipticity parameter for the elliptical Gaussian beam. Note Note that $q = 1$ is axisymmetric [see equation (29)]. q is also the ratio of the major and minor axes of the ellipse.	1.05 and 1

However, we can simplify the problem with a few approximations. First, we assume that the only effect the $\tilde{h}_k$ terms of equations (20)–(22) have on the power spectrum is to damp the resulting bias by a factor of $\langle|\tilde{h}_k|^2\rangle$, where the average is over all pixels of the sky. The phase of $\tilde{h}_k$ across the sky, and its coupling to the temperature sky, will dictate whether or not the spurious polarization is of an E-mode or a B-mode form, and therefore we expect this approximation to give an indication of the amplitude of the effect. As we do not expect the scan strategy to correlate with the temperature sky, we assume that half the resulting bias power will be of E-mode form and half of B-mode form. The temperature terms in the spurious polarization will result in an error on the B-mode power spectrum whose size is proportional to the temperature power spectrum. In equation (20), the temperature field is convolved with the axisymmetric component of the beam. Therefore, the resulting bias will be proportional to $B_\ell^2 C_\ell^T$, where $B_\ell = \sqrt{\frac{4\pi}{2\ell+1}} b_{\ell 0}$ is the smoothing function due to the beam. The differential pointing is dependent on the gradient of the convolved temperature sky and therefore the bias will be proportional to $\ell^2 B_\ell^2 C_\ell^T$. The differential ellipticity is dependent on the temperature field directly and the resulting bias will be proportional to C_ℓ^T. For the systematic error terms, we simply take the modulus squared. We provide justification for, and examine the impact of, these approximations in Appendix A. In Section 3, we demonstrate with full TOD simulations the accuracy of the approximations for a selection of representative scan strategies.

With the approximations described above, we find the following expressions for the bias on the B-mode power spectrum resulting from the systematic effects that we have considered:

$$\Delta\tilde{C}_\ell^{\rm BBg} = \frac{1}{8}\langle|\tilde{h}_2|^2\rangle\,|\delta g_1 + \mathrm{i}\delta g_2|^2\, B_\ell^2 C_\ell^{TT}, \tag{23}$$

$$\Delta\tilde{C}_\ell^{\rm BBp} = \frac{1}{32}\langle|\tilde{h}_1|^2\rangle\left|\rho_1 \mathrm{e}^{\mathrm{i}\chi_1} + \rho_2 \mathrm{e}^{\mathrm{i}(\chi_2+\pi/4)}\right|^2 \ell^2 B_\ell^2 C_\ell^{TT}, + \frac{1}{32}\langle|\tilde{h}_3|^2\rangle\left|\rho_1 \mathrm{e}^{-\mathrm{i}\chi_1} + \rho_2 \mathrm{e}^{-\mathrm{i}(\chi_2-3\pi/4)}\right|^2 \ell^2 B_\ell^2 C_\ell^{TT} \tag{24}$$

$$\Delta\tilde{C}_\ell^{\rm BBe} = \frac{4\pi}{4(2\ell+1)}\left|\Im\left[\delta b^1_{\ell 2} + \delta b^2_{\ell 2}\right]\right|^2 C_\ell^{TT} + \frac{4\pi}{8(2\ell+1)}\langle|\tilde{h}_4|^2\rangle\left|\delta b^1_{\ell 2} - \delta b^2_{\ell 2}\right|^2 C_\ell^{TT}. \tag{25}$$

Finally, we must also consider the beam deconvolution, as the reconstructed polarization map will be smoothed with the beam. When analysing a real experiment, the recovered B-mode power spectrum will be deconvolved for the beam. To take this into account, we divide equations (23)–(25) by B_ℓ^2 giving us

$$\Delta C_\ell^{\rm BBg} = \frac{1}{8}\langle|\tilde{h}_2|^2\rangle\,|\delta g_1 + \mathrm{i}\delta g_2|^2\, C_\ell^{TT}, \tag{26}$$

$$\Delta C_\ell^{\rm BBp} = \frac{1}{32}\langle|\tilde{h}_1|^2\rangle\left|\rho_1 \mathrm{e}^{\mathrm{i}\chi_1} + \rho_2 \mathrm{e}^{\mathrm{i}(\chi_2+\pi/4)}\right|^2 \ell^2 C_\ell^{TT} + \frac{1}{32}\langle|\tilde{h}_3|^2\rangle\left|\rho_1 \mathrm{e}^{-\mathrm{i}\chi_1} + \rho_2 \mathrm{e}^{-\mathrm{i}(\chi_2-3\pi/4)}\right|^2 \ell^2 C_\ell^{TT}, \tag{27}$$

$$\Delta C_\ell^{\rm BBe} = \frac{1}{4}\left|\Im\left[\frac{\delta b^1_{\ell 2} + \delta b^2_{\ell 2}}{b_{\ell 0}}\right]\right|^2 C_\ell^{TT} + \frac{1}{8}\langle|\tilde{h}_4|^2\rangle\left|\frac{\delta b^1_{\ell 2} - \delta b^2_{\ell 2}}{b_{\ell 0}}\right|^2 C_\ell^{TT}, \tag{28}$$

where the various terms are described in Table 1. We can immediately see the effect that a good scan strategy can have on mitigating systematic effects. By providing us with a range of instrument orientations, $|\tilde{h}_n|$, where $n \neq 0$, will be lowered for each pixel. This, in turn, reduces the impact of the systematics on the recovered power spectrum.

We note that a differential ellipticity of the beams within a detector pair can couple temperature to polarization with a spin-2 systematic effect [see equation (14)]. This means that no scan strategy can mitigate the effects of this systematic error. It has been shown previously (O'Dea et al. 2007; Shimon et al. 2008; Wallis et al. 2014) that if the orientation of the ellipticity is in the same direction or perpendicular to the polarization sensitivity, then this systematic effect will only couple temperature fluctuations to E-mode polarization. Any misalignment, however, will couple to B modes. This can be seen in the first term of equation (28) as the imaginary part of $\delta b_{\ell 2}$ coupling temperature power to B-mode polarization. The second term of equation (28) does allow coupling between temperature fluctuations and B-mode polarization regardless of the orientation of the ellipticity as long as the two detector pairs have different differential ellipticity. However, this effect can be mitigated by the scan strategy, as a result of the $\langle|\tilde{h}_4|^2\rangle$ factor.

Table 2. Observational parameters used to generate the scan strategies for the simulations described in Section 3.

Scan	Boresight angle (β)	Precession angle (α)	Spin period ($T_{\rm spin}$)	Precession period ($T_{\rm prec}$)
Planck	85°	7.5°	1 min	6 months
WMAP	70°	22.5°	129 s	1 h
EPIC	50°	45°	1 min	3 h

3 TEMPERATURE LEAKAGE SIMULATIONS

Equations (26)–(28) provide a fast method to predict the contamination in the recovered B-mode power spectrum for a given set of systematics and a specified scan strategy. However, in deriving these equations, a number of approximations were made. In particular, our derivation assumes that the systematics contribute to the polarization leakage only to first order in the size of the systematic. We also assumed that the effect of the scan strategy in mitigating the systematic can be modelled as a simple damping of the power spectrum and therefore does not couple multiple temperature ℓ modes on to a single B-mode scale. In this section, we perform full timeline simulations to demonstrate that equations (26)–(28) nevertheless provide an accurate prediction for the effect of the systematics on the B-mode power spectrum for a selection of scan strategies.

We create TOD simulations for two detector pairs, one 'instrument-Q' detector and one 'instrument-U' detector with different systematics. We consider the scan strategies adopted for the *Planck* (Planck Collaboration I 2011) and *WMAP* (Bennett et al. 2003) satellites. For the *WMAP* case, we simply use the orientations of the telescope ignoring any effects of differential measurements from the two sky directions present in *WMAP*. In addition, we consider the scan strategy suggested for the proposed Experimental Probe of Inflationary Cosmology (EPIC) satellite (Bock et al. 2009). The parameters used to model these scan strategies are listed in Table 2. The input signal for our simulations consists of a fiducial set of CMB power spectra with parameters: $\Omega_{\rm b} = 0.04612$, $\Omega_{\rm c} = 0.233$, $\Omega_\Lambda = 0.721$, $H_0 = 70$ kms^{-1}Mpc^{-1}, $\tau = 0.09$ and $n_{\rm s} = 0.96$. An input tensor-to-scalar ratio of $r = 0.1$ was used for all simulations and a lensing B-mode contribution was included. The input CMB power spectra were created with CAMB (Lewis & Challinor 2011) and we used the HEALPIX[3] package (Górski et al. 2005) to create simulated maps, and to estimate power spectra.

In Fig. 2, we show the hit maps and maps of $|\tilde{h}_n|$ for $n = \{1, 2, 3, 4\}$ for 1 yr of observations at a data sampling rate of 500 Hz. These maps have been constructed using HEALPIX resolution parameter, $N_{\rm side} = 2048$, corresponding to a pixel size of ∼2.7 arcmin. The lower these h values are, the better the scan strategy will be at mitigating different systematics. From equations (26)–(28) we can see that the average value of these maps acts a scaling factor for the leakage from temperature power spectrum to B-mode polarization power spectrum.

For each scan strategy, we simulated the effects of each systematic (differential gain, pointing, and ellipticity) individually assuming the parameters listed in Table 1. For all the simulations, except for the differential ellipticity simulations, a Gaussian beam with a full width at half-maximum (FWHM) of 7 arcmin was used. To assess the differential ellipticity mitigation, an elliptical Gaussian beam was used:

$$B(\theta, \phi) = \frac{1}{2\pi q \sigma^2} {\rm e}^{-\frac{\theta^2}{2\sigma^2}(\cos^2\phi + q^{-1}\sin^2\phi)}. \quad (29)$$

In order to separately assess the impact of the two contributions to equation (28), we run two sets of simulations. The effect described by the first term in equation (28) is simulated by each of the four detectors having a beam, described by equation (29), with $q = 1.05$, but with the beam such that the ellipticity is rotated by $\pi/4$ with respect to the polarization sensitivity direction. A beam of this type has the property that the second azimuthal mode of the spherical harmonic decomposition is imaginary. Such a setup will therefore strongly contribute a systematic of the type corresponding to the first term of equation (28). As both the 'instrument-Q' and 'instrument-U' detectors have the same differential ellipticity in this setup, there will be no systematic of the type corresponding to the second term in equation (28).

The second term of equation (28) is non-zero when the differential ellipticities within the two detector pairs are different. We create this effect by simulating both detectors within one pair to have a symmetric Gaussian beam of FWHM = 7 arcmin, while the detectors of the other pair are modelled as having elliptical beams, aligned with the polarization sensitivity direction, and described by equation (29). Both detectors in this latter pair are set up to have $\sigma = 3$ and $q = 1.05$, but for one of these, the beam is rotated by $\pi/2$ in order to create the required differential ellipticity.

The results from these simulations are shown in Fig. 3 in terms of the B-mode power spectrum recovered from Q and U maps which are constructed from the TOD using a simple binned map-making algorithm. We plot the recovered power spectrum for each of the systematics considered, and for each of the three scan strategies tested. In this figure, we have also plotted the theoretical predictions for the spurious signal from equations (26)–(28). We see that the theoretical predictions are accurate for $\ell \lesssim 1000$ which, for a beam of FHWM = 7 arcmin, is approaching the beam scale. The purpose of this plot is to show that the analytical predictions are consistent with the simulations therefore justifying their validity.

4 SCAN-STRATEGY PARAMETER SPACE

4.1 Scan-strategy parameters

Having established the accuracy of equations (26)–(28) for a representative selection of scans, we now proceed to use these expressions to quantify the effectiveness of the scan strategy to mitigate leakage as a function of the observational parameters that define it.

The model we adopt to describe a satellite scan uses five parameters. First, the telescope will spin about the major axis of the satellite. We denote the time period of this rotation as $T_{\rm spin}$. The boresight of the telescope will be at an angle to the spin axis which we call β. This spin axis is then allowed to precess around an axis. We choose this precession axis to be the extended line passing through the Sun and the Earth, presuming that the satellite is placed at the second Lagrange point (L2) of the Earth–Sun system. This arrangement therefore allows the telescope to be facing away from the Sun as much as possible. The angle between the spin axis and the precession axis is denoted by α, and the time period for the precession is $T_{\rm prec}$. A schematic diagram of this setup is shown in Fig. 4. Finally, the satellite will sample the sky at a frequency of $f_{\rm samp}$.

At first glance, this seems to suggest that there are five free parameters to describe the scan strategy. However, there are a number

[3] See http://healpix.sourceforge.net

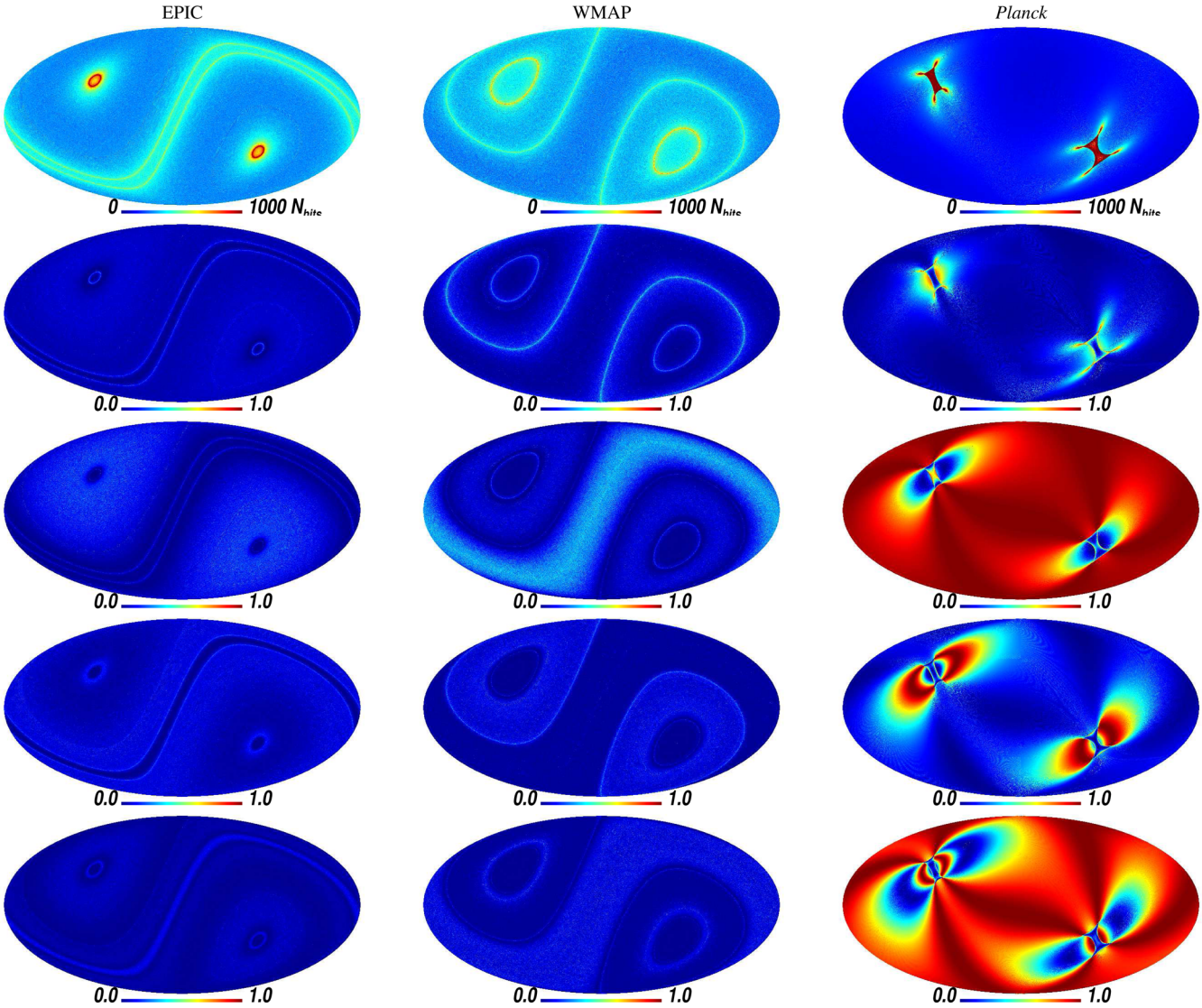

Figure 2. Top row: the hit maps for the EPIC (left), *WMAP* (centre) and *Planck* (right) scan strategies used in the simulations at $N_{\rm side} = 2048$. Lower rows: maps of $|\tilde{h}_n|^2$, defined in Table 1, for $n = \{1, 2, 3, 4\}$, for the different scan strategies. The lower the value of $|\tilde{h}_n|^2$, the smaller the temperature to polarization leakage is. Note that in our formalism $\langle|\tilde{h}_2|^2\rangle = \langle(\frac{1}{N_{\rm hits}}\sum_j \cos(2\psi_j))^2\rangle + \langle(\frac{1}{N_{\rm hits}}\sum_j \sin(2\psi_j))^2\rangle$. This is the same quantity as that plotted in fig. 3.5 of Bock et al. (2009). All the plots are a Mollweide projection in Galactic coordinates.

of additional constrains one may wish to enforce. The first and most obvious constraint is that the telescope must observe the entire sky. This requires that

$$\alpha + \beta > 90^\circ. \tag{30}$$

This hard limit of 90° is only strictly true for detectors in the centre of the focal plane, as the effective values of β for each detector will be different. For this reason, it is common to set these values to sum to 95° as done in this work.

Further constraints arise from considering the spin rate of the telescope. One can envisage three potential constraints. First, one may wish to ensure that neighbouring rings on the sky are mapped sequentially. As the telescope spins, it maps out a ring of radius β on the sky. The precession of the telescope means that the next ring will be displaced from the preceding one. One may then wish to ensure that the spatial separation of sequential rings is less than some maximum separation which may be chosen to be, e.g. a fraction of the beam width, or a fraction of the field of view. Such a constraint would then allow for continuous mapping of the sky. This requirement places an upper bound on the ratio $T_{\rm spin}/T_{\rm prec}$ of

$$\frac{T_{\rm spin}}{T_{\rm prec}} < \frac{\theta_\perp}{2\pi \sin\alpha}, \tag{31}$$

where $\theta_\perp$ is the desired separation of sequentially mapped rings.

A second consideration that impacts the choice of $T_{\rm spin}$ is the potential requirement that the scan speed is fast enough such that the large-scale modes in the sky are not confused with gain drifts in the detectors creating '$1/f$ noise'. The noise power spectra of detectors are in general not white. They can often be modelled by the sum of a white component and an additional $1/f$ component that becomes important on long time-scales. The transition point is often termed the knee frequency of the $1/f$ noise, $f_{\rm knee}$. Delabrouille et al. (1998) previously investigated the impact of scan strategies on the resulting noise level of a map in the presence of $1/f$ noise. Here, we place a simple requirement on $T_{\rm spin}$: we require that a particular scale of interest on the sky, quantified by $\ell_{\rm min}$, appears in

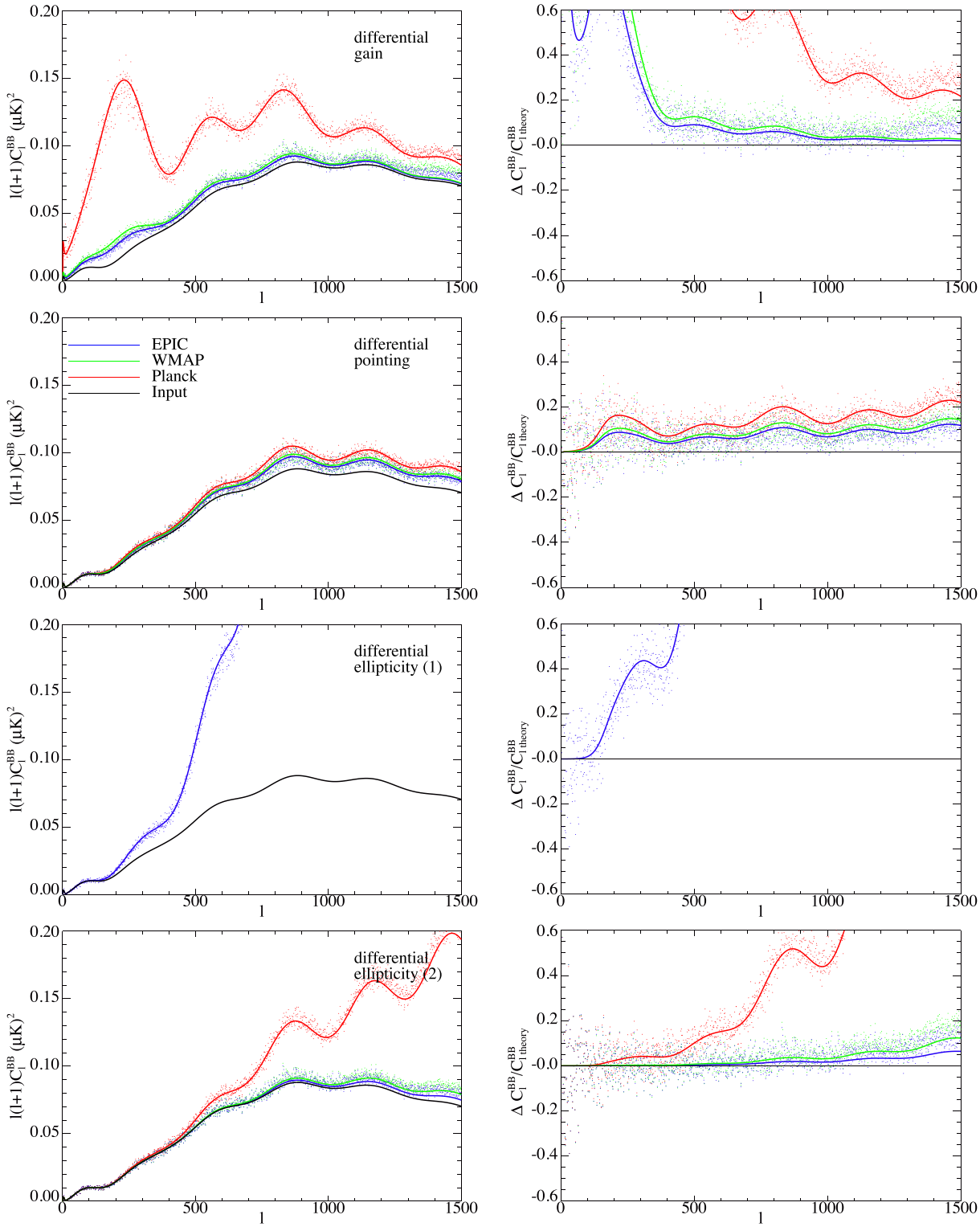

Figure 3. The recovered B-mode power spectrum from simulations including systematic effects when using the *Planck*, *WMAP* and EPIC scan strategies (shown in red, green and blue, respectively). The points show the result for one simulation – see Section 3 for a full description. The left-hand panels show the recovered power spectra alongside the input spectra (shown as the smooth black curves). The right-hand panels show the fractional bias in the recovered spectra. The simulations included differential gain of 1 per cent (top row), differential pointing of 1.5 per cent (second row), differential ellipticity of 5 per cent in both detector pairs [third row, to test the first term of equation (28)] and differential ellipticity in only one detector pair [bottom row, to test the second term in equation (28)]. Also plotted are the predictions from equations (26)–(28) for the systematic effects showing good agreement with the simulated results. This plot demonstrates the accuracy of the analytic predictions for the systematics. Note that in some cases, the levels of the systematics were deliberately increased in order to clearly demonstrate the accuracy of the predictions. A tensor-to-scalar ratio of $r = 0.1$ was used in the simulations along with a fiducial CMB temperature power spectrum. Note that the spurious B mode produced by the effect corresponding to the first term in equation (28) is independent of the scan strategy. We, therefore, plot the result from just one simulation in the third row of panels.

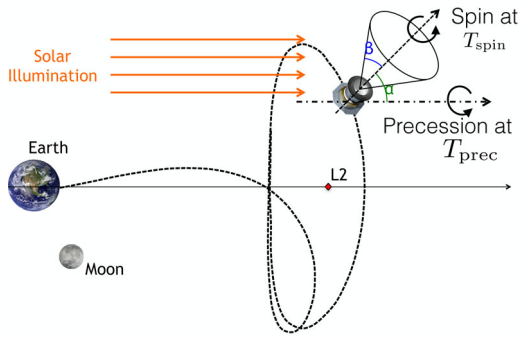

Figure 4. Schematic diagram describing the observational parameters used to define the scan strategies.

the timestream at least a factor of F in frequency higher than $f_{\rm knee}$. This places an upper bound on the value of $T_{\rm spin}$:

$$T_{\rm spin} < \frac{2\ell_{\rm min}\sin\beta}{F f_{\rm knee}}. \tag{32}$$

In this work, we set $\ell_{\rm min} = 2$, $f_{\rm knee} = 0.01$ Hz (consistent with a slight improvement of the *Planck* 143 GHz detector; Planck HFI Core Team et al. 2011) and $F = 2$.

In addition to the effects of $1/f$ noise, bolometers can also suffer if the signal varies on very short time-scales. Bolometers require a finite amount of time to respond to a change in the incoming radiation. The response of a bolometer, d, to a sudden impulse of power as a function of time, t, is

$$d(t) \propto {\rm e}^{-t/t_\star}, \tag{33}$$

where $t_\star$ is the time constant of the detector (Delabrouille et al. 1998). It is desirable therefore to ensure that the telescope scans slow enough such that the telescope pointing only moves a fraction, p, of the beam FWHM, $\theta_{\rm FWHM}$, in a time $t_\star$. This places a lower bound on the spin period:

$$T_{\rm spin} > \frac{2\pi t_\star \sin\beta}{p\theta_{\rm FWHM}}. \tag{34}$$

If we set $t_\star = 1$ ms (consistent with the *Planck* CMB channels; Planck HFI Core Team et al. 2011), $p = 1/4$ and $\theta_{\rm FWHM} = 5.0$ arcmin, then this places a lower bound on $T_{\rm spin}$, that is a factor of 10 below the upper bound imposed by the requirement to avoid $1/f$ noise.

Finally, we require that the sampling frequency $f_{\rm samp}$ must be fast enough so that the beam width is fully sampled. We quantify this by requiring that the telescope must not move further than some fraction of the beam width, W, between samples. This translates to a lower bound on the sampling frequency of

$$f_{\rm samp} > \frac{2\pi\sin\beta}{W\theta_{\rm FWHM}T_{\rm spin}}. \tag{35}$$

In this work, we set $W = 1/4$.

4.2 Practical constraints on scan strategies

In addition to the science-driven requirements detailed above, one also needs to consider a number of practical constraints which also limit the possible scan-strategy parameter values. The exact values considered in this section for the practical constraints are used as an example. The values are reasonable constraints at the time of writing and may be relaxed in future.

Due to computing considerations, large values of $T_{\rm spin}$ are easier to implement in our scan-strategy simulations; as the higher spin periods lead to lower sampling frequencies, this leads to fewer pointings to calculate. In the following work, we therefore choose $T_{\rm spin}$ to be the largest allowed value, given the chosen joint constraints on it and the other parameters. Additionally, given that higher sampling rates are problematic from the point of view of data transfer considerations, in all of our simulations we choose the lowest possible value of $f_{\rm samp}$ given the constraint of equation (35).

One practical constraint that must be considered when choosing a scan strategy is the required fuel to maintain the precession. The required torque to maintain a gyroscopic precession is

$$\tau = I_{zz}\omega_{\rm prec}\omega_{\rm spin}\sin\alpha, \tag{36}$$

where I_{zz} is the moment of inertia of the telescope about the spin axis, $\omega_{\rm prec} = 2\pi/T_{\rm prec}$ is the angular velocity of the precession and $\omega_{\rm spin} = 2\pi/T_{\rm spin}$ is the angular velocity of the telescope spin (Feynman 1977; Markley et al. 2005). This leads to a total velocity impulsion of

$$\Delta v = \int {\rm d}t \frac{\tau}{M_{\rm sat}R_{\rm lever}} \tag{37}$$

$$= \frac{\tau T_{\rm mission}}{M_{\rm sat}R_{\rm lever}}, \tag{38}$$

where $M_{\rm sat}$ is the mass of the satellite, $R_{\rm lever}$ is the distance of the rocket from the spin axis and $T_{\rm mission}$ is the lifetime of the mission. In the upper panels of Fig. 5, we plot the required impulsion for a telescope using typical values for an experiment, $I_{zz} = 2000\,{\rm kg\,m^2}$, $M_{\rm sat} = 2000\,{\rm kg}$, $R_{\rm lever} = 1.5\,{\rm m}$ and $T_{\rm mission} = 4\,{\rm yr}$. We show the results for a range of $T_{\rm prec}$ and α-values and we have set $\alpha + \beta = 95^\circ$ in all cases.

We present results on the required impulsion for two cases. The first is the case where $T_{\rm spin}$ is chosen such that it meets the requirement on continuous mapping [equation (31)], where we set $\theta_\perp = 3$ arcmin. The second is for the case where $T_{\rm spin}$ is chosen according to the requirement to limit the impact of low-frequency $1/f$ detector noise [equation (32)]. For this latter case, we set $\ell_{\rm min} = 2$, $F = 2$ and $f_{\rm knee} = 0.01$ Hz.

The second major practical concern is the implications that different scan strategies have for the required data rate. Higher sampling frequencies obviously require a faster data transfer to the earth. The required data rate per detector is proportional to the sampling frequency and hence,

$$\text{data rate} = N_{\rm b} f_{\rm samp}, \tag{39}$$

where $N_{\rm b}$ is the number of bits per sample, which we choose to be 8. In the lower panels of Fig. 5, we present the required data rate per detector as a function of $T_{\rm prec}$ and α. As for the investigation of the required impulsion discussed above, we present our results for two possible ways of choosing $T_{\rm spin}$, according to either equation (31) or equation (32).

For comparison, we also plot contours of 'reasonable values' for the impulsion and data rate. We plot the contours of impulsion requirements for $\Delta v = 48$, 113 and 290 ms^{-1}. These correspond to the possible impulsion values after having obtained 'small', 'medium' and 'large' Lissajou orbits centred around L2. This assumes that the satellite will have a fixed amount of fuel for both orbit injection and to drive the scan. We have here subtracted the fuel required to achieve the respective orbits. For the data rate plots, we show a contour of data rate per detector corresponding to a total data rate of 20 Mbps for 4800 detectors.

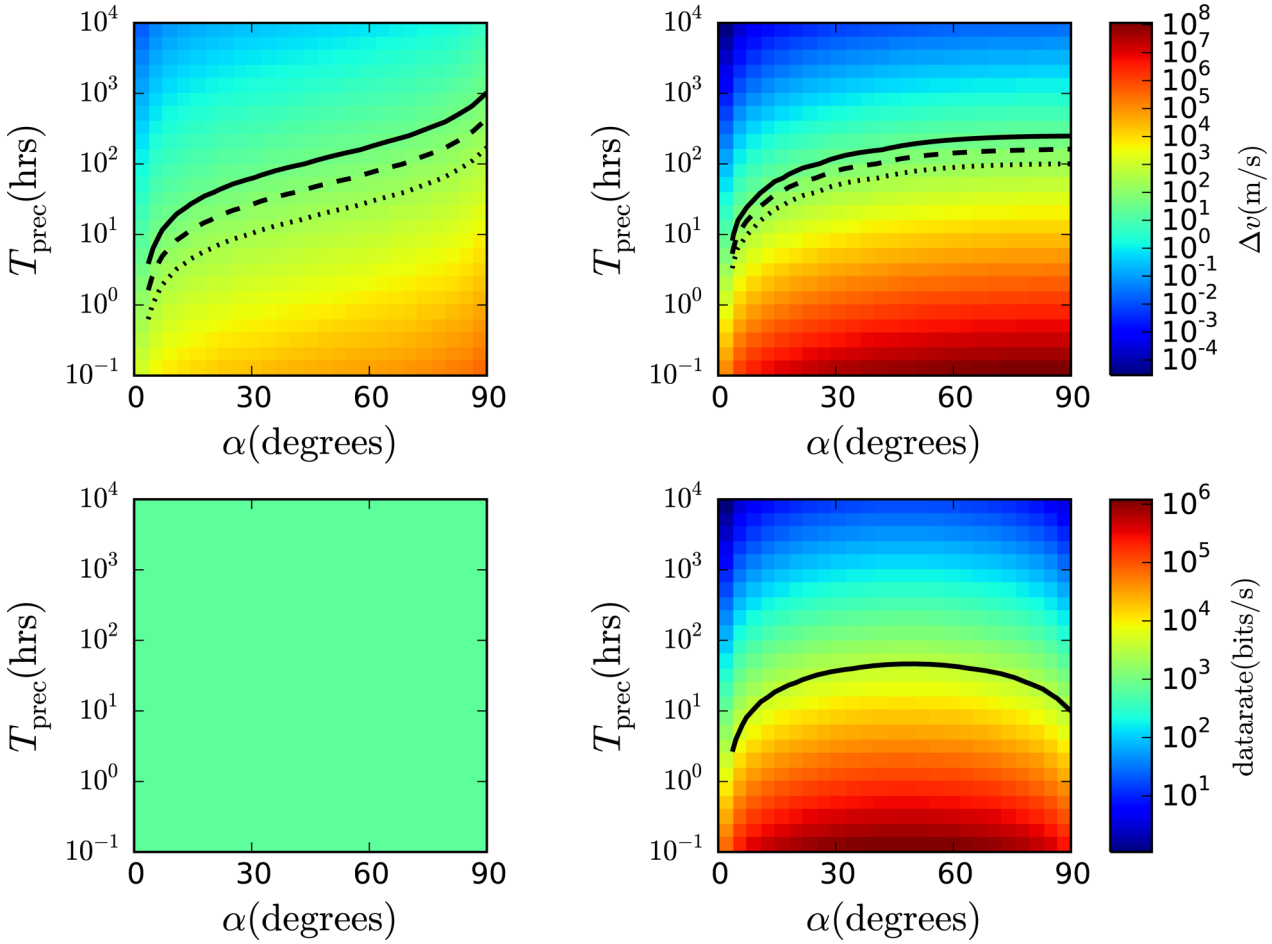

Figure 5. Upper panels: we plot the required impulsion to maintain the scan strategies as a function of the scan parameters. In the left-hand panel, we have used the $T_{\rm spin}$ constraint from equation (32). The panel on the right shows the result when the constraint from equation (31) is used. Overplotted are contours of $\Delta v = 48$, 113 and 290 m s^{-1} to show reasonable impulsion values. These correspond to the possible impulsion values after achieving a small, medium and large L2 orbit (shown with solid, dashed and dotted lines, respectively). Lower panels: we plot the data rate per detector requirements given the required sampling frequency. We have used the $T_{\rm spin}$ constraint from equation (32) on the left and the constraint from equation (31) on the right. See Section 4.2 for details. Overplotted is a contour of constant data rate corresponding to a total data rate of 20 Mbps for 4800 detectors. As the $T_{\rm spin}$ constraint from equation (32) requires all the scan strategies to scan at the same speed, and the sampling frequency is set by the scan speed, the data rate is therefore constant for all values of α and $T_{\rm prec}$.

The telescope pointing with respect to the Sun is also of significant importance. To minimize far sidelobe pick up of the Sun, the telescope must never be pointed too close to the Sun. For this reason, we have set $\alpha + \beta = 95^\circ$. This means our telescope never points closer than 85°. However, the Sun's influence can also place constraints on α itself. As α is the angle between the spin axis and the Sun–Earth line, large values of α mean the Sun will be shining on the side of the telescope at a more acute angle. Therefore, large values of α must also be accommodated with more effective heat shielding. Solar panels must be located on the warm service module rather than on the cold payload. A high value of the precession angle α results in less efficient orientation of the solar panels with respect to the Sun. Therefore, a more sophisticated setup for the solar panels may be required.

The data transfer antenna sets a limit on the maximum precession angle allowed. The earth aspect angle $\theta_{\rm earth}$ cannot exceed a certain value to allow the antenna to point towards the earth. Here, we set $\theta_{\rm earth} \leq 62^\circ$ as currently available antenna choices set this limit. If the limit was changed, the possible scan strategies would increase. This aspect angle is increased by both the precession angle and the position of the satellite:

$$\theta_{\rm earth} = \alpha + \theta_{\rm orbit}, \tag{40}$$

$$\leq 62^\circ, \tag{41}$$

$$\theta_{\rm orbit} = \arctan\left(\frac{R_{\rm orbit}^{\rm max}}{R_{\rm L2}}\right), \tag{42}$$

where $R_{\rm orbit}$ is the radius of the satellite around L2 and $R_{\rm L2}$ is the distance of L2 from the earth. Therefore, if the satellite is placed in a smaller orbit around L2 then a larger precession angle α will be possible. However, the fuel required to place the satellite in this smaller orbit will be larger which leaves us less fuel to drive the scan strategy.

The results from this assessment of practical considerations suggest that a large fraction of parameter space is difficult to achieve in practice. The reader should therefore bear in mind Fig. 5 when interpreting the results, displayed in Fig. 7, regarding the impact of different scan strategies on mitigating systematics which we now go on to discuss.

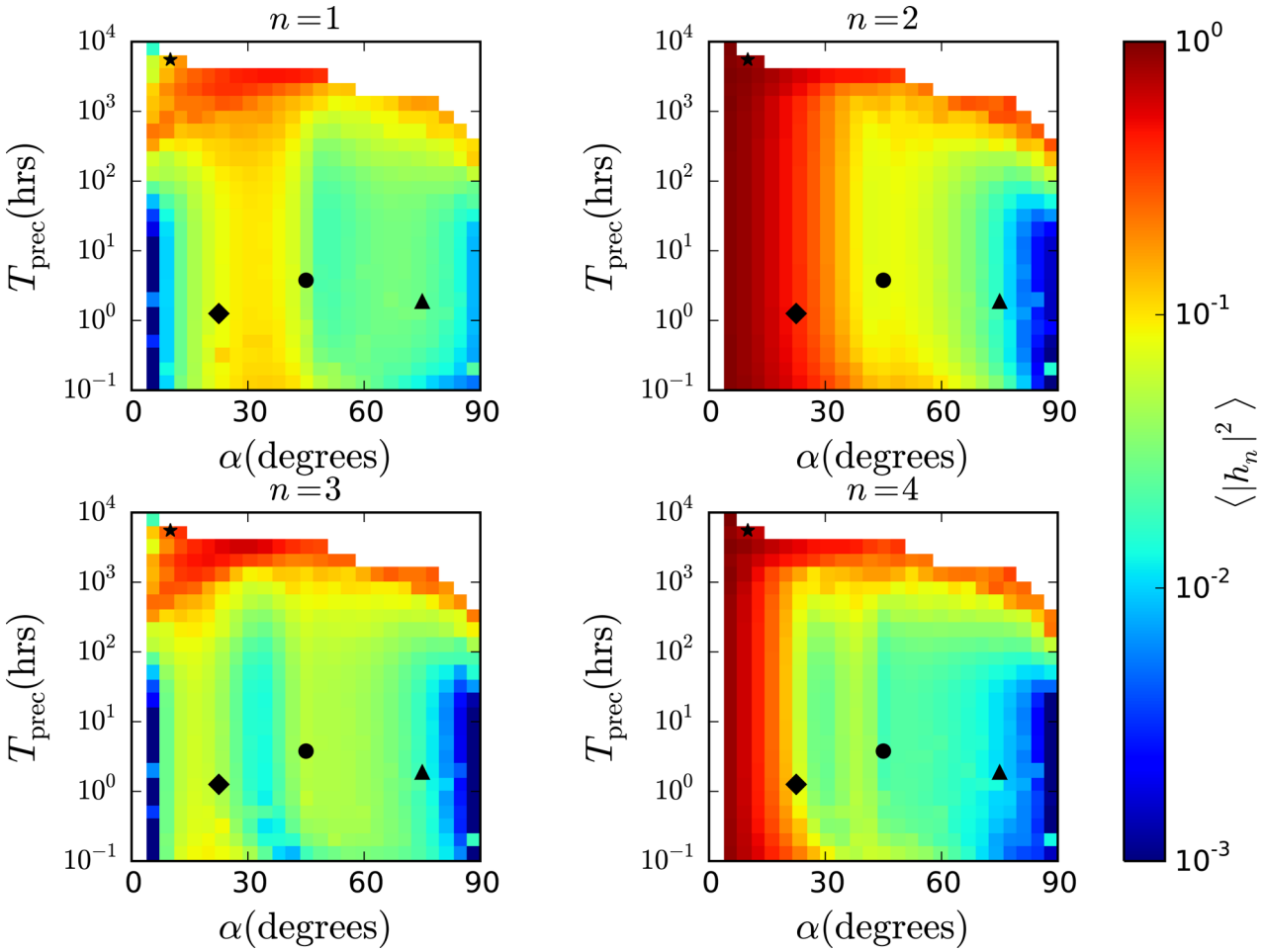

Figure 6. We plot the values of $\langle|\tilde{h}_n|^2\rangle$, used in equations (26)–(28) as a function of the scan-strategy parameters. The $\langle|\tilde{h}_n|^2\rangle$ values for $n = \{1, 2, 3, 4\}$ are displayed in the top left, top right, lower left and lower right panels, respectively. The lower the value of $\langle|\tilde{h}_n|^2\rangle$, the smaller the temperature to polarization leakage is for a particular systematic error in the experiment. $\langle|\tilde{h}_2|^2\rangle$ is important for mitigating differential gain; $\langle|\tilde{h}_1|^2\rangle$ and $\langle|\tilde{h}_3|^2\rangle$ are important for mitigating differential pointing; and finally $\langle|\tilde{h}_4|^2\rangle$ is important for mitigating the difference between the differential ellipticity. White regions show areas where the entire sky is not observed in 1 yr. In each panel, we indicate the positions of the *Planck*, *WMAP*, EPIC and LiteBIRD scan strategies with a star, a diamond, a circle and a triangle, respectively.

4.3 Error on the main science goals

The analysis of Section 2 provides a quick but accurate method to predict the error on the recovered B-mode polarization power spectrum due to certain systematic errors and given certain features of the scan strategy. We have additionally developed a fast scan-strategy simulation code that calculates the pointing and orientation of the telescope with respect to north for a given set of scan-strategy parameters over 1 yr of observations. This pointing information can then be used to calculate the $\langle|\tilde{h}_n|^2\rangle$ values for that particular set of scan-strategy parameters. The calculated values can then be used to predict the error on the recovered B-mode power spectrum using equations (26)–(28).

In Fig. 6, we plot the $\langle|\tilde{h}_n|^2\rangle$ values as a function of the scan-strategy parameters, α and $T_{\rm prec}$. In all cases, we have overplotted the positions of the *Planck*, *WMAP* and proposed EPIC scan strategies. We have also overplotted an example LiteBIRD scan strategy on the grid for reference. It should be noted that the baseline LiteBIRD design includes a rotating HWP in the optical chain which will improve both the ability to mitigate systematic effects and the noise properties of the experiment (Matsumura et al. 2014). In implementing the scan strategies for each point in the $\{\alpha$–$T_{\rm prec}\}$ parameter space, we have made a number of choices for the values of the other observational parameters. These choices were motivated by the considerations outlined in Section 4.1. First, we have set $\alpha + \beta = 95^\circ$. We have checked that this choice has little impact on the results within $\pm 5^\circ$. We therefore choose the angle sum to be similar to other scan strategies in the literature. In particular, both the *Planck* and *WMAP* scan strategies have $\alpha + \beta = 92.5^\circ$ while the proposed EPIC scan strategy has the sum equalling 95°.

We chose the value of $T_{\rm spin}$ such that it satisfies the requirement of equation (32). As before, we set $\ell_{\rm min} = 2$, $F = 2$ and $f_{\rm knee} = 0.01$ Hz. When the constraint of equation (31) was used, for $T_{\rm prec} \lesssim 10^2$ h, the $\langle|\tilde{h}_n|^2\rangle$ values showed no discernible change. The fact that the h-values were unchanged is to be expected because $T_{\rm spin} \ll T_{\rm prec}$ in both cases. Finally, we have chosen $f_{\rm samp}$ such that it fulfils the requirement of equation (35), for a $\theta_{\rm FWHM} = 5$ arcmin beam width.

From equations (26) to (28), we can see that the lower the values of $\langle|\tilde{h}_n|^2\rangle$, the smaller the temperature to polarization leakage is for a particular systematic error in the experiment. $\langle|\tilde{h}_2|^2\rangle$ is important for mitigating differential gain, $\langle|\tilde{h}_1|^2\rangle$ and $\langle|\tilde{h}_3|^2\rangle$ are important for

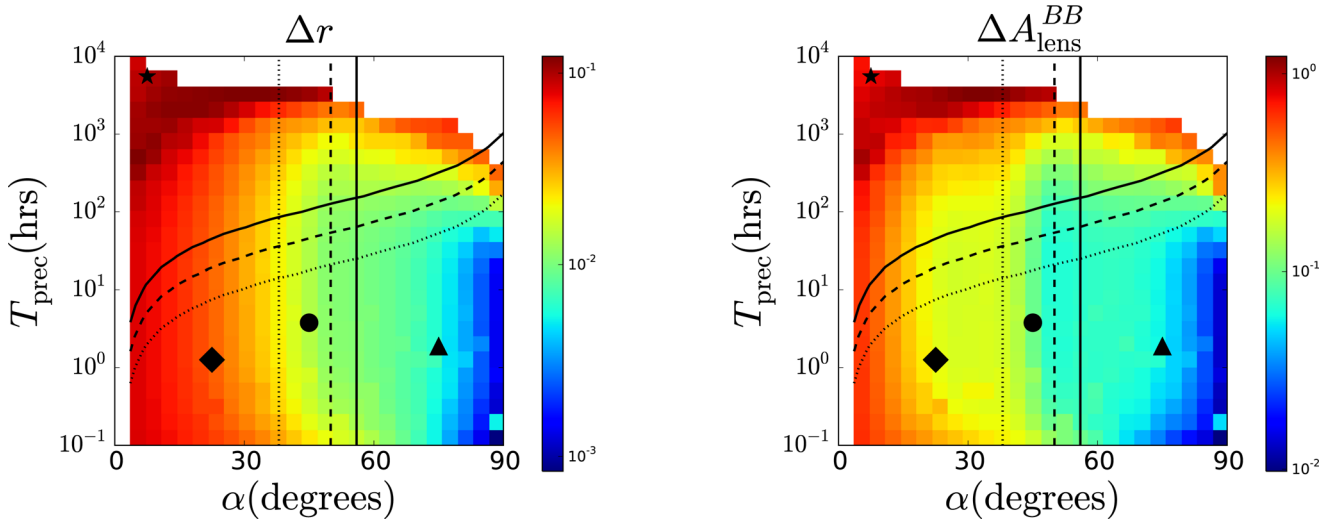

Figure 7. Left-hand panel: the error on the tensor-to-scalar ratio r as a function of the scan-strategy parameters (see Section 4.3 for details). A differential gain of 0.2 per cent, a differential pointing of 2 per cent and a differential ellipticity of 5 per cent in one detector aligned with the polarization sensitivity were assumed. Right-hand panel: the same as the left-hand panel but for the lensing amplitude parameter $A^{\rm BB}_{\rm lens}$. Note that the morphology of the two plots is the same but the amplitude is different. White regions show areas where the entire sky is not observed in 1 yr. In each panel, we indicate the positions of the *Planck*, *WMAP*, EPIC and LiteBIRD scan strategies with a star, a diamond, a circle and a triangle, respectively. The overplotted lines give an indication of the likely restrictions on scan-strategy parameter space due to the maximum fuel capacity of the satellite and the maximum aspect angle of the satellite with respect to the Earth, which is limited by data transmission requirements. Regions of parameter space below the curved lines require more fuel to drive the scan strategy than what is likely to be available after injection into orbit around L2. The solid, dashed and dotted lines correspond to injection into small, medium and large Lissajou L2 orbits, respectively (see Section 5 for details). The vertical lines indicate the likely maximum possible values for α in order to meet the data transfer requirements on the satellite aspect angle. Once again, the solid, dashed and dotted lines correspond to small, medium and large Lissajou L2 orbits, respectively.

mitigating differential pointing, and finally $\langle|\tilde{h}_4|^2\rangle$ is important for mitigating any difference in the differential ellipticities of different detector pairs [see the second term of the right-hand side of equation (28)]. The results of Fig. 6 show that the choice of $T_{\rm prec}$ has little impact on the $\langle|\tilde{h}_n|^2\rangle$ values unless $T_{\rm prec} \gtrsim 20$ h. This can be understood by considering the other time-scales in the problem. With $T_{\rm prec} \lesssim 20$ h, then $T_{\rm spin} \ll T_{\rm prec} \ll 1$ yr meaning that this would have little effect on the quality of the scan strategy. If the value of $T_{\rm prec}$ is too large then the scan strategy cannot observe the entire sky in 1 yr. This region of parameter space is shown in white in Fig. 6.

Fig. 6 does show, however, that the precession angle, α, has a significant impact on the quality of the scan strategy. A smaller boresight angle (β) will result in the satellite scanning in smaller circles. Given the constraint $\alpha + \beta = 95^\circ$, a smaller value of β corresponds to a larger precession angle α. Scanning in smaller circles generally creates a larger range of orientations for each pixel and thus improves the quality of the scan strategy by lowering the $\langle|\tilde{h}_n|^2\rangle$ values, where n is even. When n is odd, scanning in larger circles results in a small range of orientation angles. However, 6 months later the scan is flipped, creating a symmetry that renders the odd terms close to zero. This symmetry is enhanced when the range of orientation angles is small, creating a deep valley in the $\langle|\tilde{h}_1|^2\rangle$ and $\langle|\tilde{h}_3|^2\rangle$ values at $\alpha \approx 5^\circ$.

Using equations (26)–(28), we can translate the $\langle|\tilde{h}_n|^2\rangle$ surfaces of Fig. 6 into estimates of the resulting error on the recovered B-mode power spectrum. To do this, we must make some assumptions regarding the levels of the systematics to include in the calculations. Apart from differential gain, we use typical values for these types of systematics as found in the BICEP2 experiment instrumental systematics paper (BICEP2 Collaboration et al. 2015). For differential gain, we note that satellite-based missions can use the CMB dipole to calibrate the bolometers, and can therefore achieve much lower levels of differential gain, of the order of 0.2 per cent (Planck Collaboration VIII 2016). Specifically, we choose a differential gain of 0.2 per cent, a differential pointing of 2 per cent of the beam FWHM and a differential ellipticity of 5 per cent corresponding to $q = 1.05$ [see equation 29)].

With these calculated errors on the recovered power spectrum, given a scan strategy, we then go on to estimate the error on the recovered cosmological parameters. We focus on two key parameters: the tensor-to-scalar ratio r, and $A^{\rm BB}_{\rm lens}$, which parametrizes the amplitude of the B-mode lensing signal, as used in The Polarbear Collaboration: P. A. R. Ade et al. (2014). In order to do this, we calculate the error on two important $C^{\rm BB}_\ell$ multipole bins. Our first bin covers the multipole range $2 \leq \ell \leq 201$. We use the error on this bin (which we call $\Delta C^{\rm BB}_{b=1}$) to assess an experiment's ability to recover an inflationary B-mode signal on large scales. We calculate the amplitude of the predicted signal in this bin (which we call $C^{\rm BB}_{b=1}$) for a cosmology where $r = 1$ and in the absence of lensing B modes. We assume the latter have been removed to make a best estimate of r. As the amplitude of the signal within this bin is simply scaled by the value of r, we can therefore find the error on the recovered value of r, which we call Δr:

$$\Delta r = \frac{\Delta C^{\rm BB}_{b=1}}{C^{\rm BB}_{b=1}}. \tag{43}$$

The other bin we consider covers the range $801 \leq \ell \leq 1000$ in order to assess our ability to recover the lensing B-mode power spectrum. We follow a similar procedure: we calculate the error on this bin ($\Delta C^{\rm BB}_{b=2}$) and the predicted value for $A^{\rm BB}_{\rm lens} = 1$ ($C^{\rm BB}_{b=2}$). As the parameter simply scales the B-mode power spectrum, the error

on $A_{\rm lens}^{\rm BB}$ will be

$$\Delta A_{\rm lens}^{\rm BB} = \frac{\Delta C_{b=2}^{\rm BB}}{C_{b=2}^{\rm BB}}. \quad (44)$$

The results are presented in Fig. 7. This figure clearly shows, as described before, that the dominant parameter in mitigating temperature to B-mode polarization leakage is the precession angle α, once $T_{\rm prec} \ll 1$ yr: as α increases the spurious signal induced in the B-mode polarization power spectrum reduces dramatically.

It should be noted that our method for predicting the temperature to B-mode leakage provides us with a worst-case scenario as we have only considered an experiment with two pairs of detectors. In a real experiment, the leakage from each detector pair will be different and in certain situations the leakage from different detector pairs could be completely uncorrelated. This would result in the overall leakage averaging to a lower value. The differential gain between detector pairs is unlikely to be correlated. However, the effects of differential pointing and differential ellipticity could conceivably be a function of the position of the detector pair in the focal plane and/or imperfections in the primary lens or mirror of the telescope. Such a scenario would result in the leakage from different detector pairs being correlated and hence not averaging to an overall lower value.

4.4 Long time-scale drifts

Before we can choose a scan strategy, it is imperative that we consider other problematic consequences a particular scan strategy can have on the final data analysis. One potential complication is the need to filter the TOD in order to remove long time-scale drifts of the detectors. These long time-scale drifts are a result of the $1/f$ noise considered in Section 4.1. In order to minimize the impact of $1/f$ noise, we required that the scan speed of the telescope should be fast enough such that the largest angular scale of interest ($\ell = 2$) appears in the TOD at a time-scale twice that of $f_{\rm knee}$. This choice could be problematic, as large values of α can lead to the telescope observing a relatively small patch of the sky for long time periods even if, over that patch, it is scanning quickly.

In data analysis, there is often a step where long time-scale drifts are removed from the TOD, in order to suppress the effects of $1/f$ noise (stripes) on the resulting map. This typically involves the use of filtering or destriping algorithms, many of which filter the TOD with a high-pass filter removing long time-scales (Delabrouille 1998; Sutton et al. 2010; Cantalupo et al. 2010). While this filtering reduces the long time-scale noise in the map, it can also remove some of the true sky signals. Filtering of true sky signal in this way is something which we would like to avoid and/or minimize. While destriping algorithms can remove the low-frequency noise persevering the signal, the effectiveness of the algorithm will depend on the scan strategy.

To fully assess the impact that the scan-strategy choice has on TOD filtering requirements in the presence of $1/f$ noise would require full TOD simulations including realistic $1/f$ noise and the subsequent application of a destriping algorithm to the simulated data. One would then need to analyse the resulting maps to investigate which scans required the least amount of filtering in order to meet the science goals. The results of this exercise would depend strongly on the choice, and implementation of, the destriping algorithm, so ideally one would use many and compare the results. Such an analysis is beyond the scope of this work. Additionally, there could well be developments in destriping algorithms before the data are collected and analysed, and one would ideally use those, as yet undeveloped, superior algorithms in such an investigation.

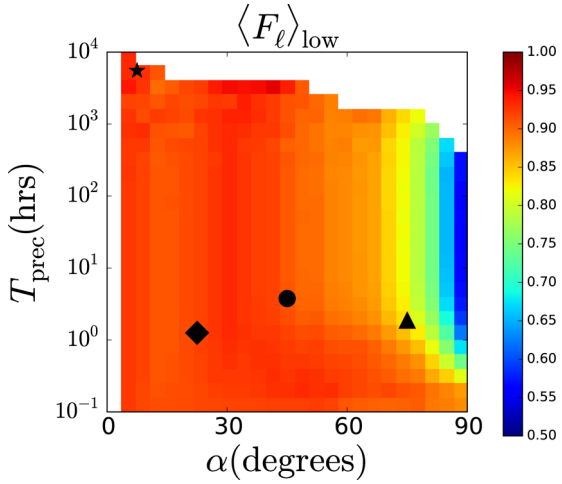

Figure 8. The average of F_ℓ [see equation (45)], over a multipole range $2 \leq \ell \leq 25$ for a naively filtered timestream for a range of scan strategies. The simulated TOD was filtered by removing the mean signal from 3 min sections of TOD. A binned temperature map was constructed from this filtered timestream and its power spectrum calculated. This procedure naively models the effect of a destriping algorithm filtering the cosmological signal. We indicate the positions of the *Planck*, *WMAP*, EPIC and LiteBIRD scan strategies with a star, a diamond, a circle and a triangle, respectively.

We can however obtain some insight on the effect that the scan strategy has on the resulting filtering requirements by implementing a naive TOD filtering for each scan. To do this, for each scan, we have performed signal only simulations of the TOD from one detector, which is only sensitive to temperature fluctuations. We have then filtered the TOD by removing the mean from 3 min sections of the TOD. We then make maps of the temperature sky using these TODs, where the input sky model only contains CMB fluctuations. The power spectrum of the reconstructed maps is calculated and we assess the result of the filtering by calculating

$$F_\ell = \frac{C_\ell^{T\,\rm meas}}{C_\ell^{T\,\rm true}}, \quad (45)$$

where $C_\ell^{T\,\rm meas}$ is the power spectrum of the map after filtering and $C_\ell^{T\,\rm true}$ is the power spectrum of the map before filtering. F_ℓ ranges from 0 to 1 – the higher the value, the less the signal has been removed. Fig. 8 shows the average of F_ℓ over the range $2 \leq \ell \leq 25$. We choose to plot this range as the large-scale power is the most affected by this type of filtering. Fig. 8 shows the regions of scan-strategy space that should be avoided in order to minimize loss of signal due to filtering. Unless $T_{\rm prec} \lesssim 1$ h, then $\alpha \lesssim 60^\circ$ is necessary to avoid filtering the TOD to a significant level.

5 CHOOSING A SCAN STRATEGY

We are now in a position, as an example, to suggest a scan strategy for the COrE++ proposal for the ESA M5 mission call. We aim to choose the scan strategy that will mitigate systematic effects most effectively given the practical constraints on possible scans outlined in Section 4.2. We examine three potential L2 orbits for the satellite.

As described in Section 4.2, there is a maximum aspect angle, of 62°, that the satellite can have with respect to the Earth, set by the antenna transmitting data to the ground. The larger the orbit, the smaller the scan precession must be [see equation (40)]. However,

Table 3. Table showing three possible orbits around L_2 and the required impulsion. We also show the implications of such orbits on the remaining fuel to drive the scan strategy and the possible precession angles given the orbit, see Section 4.2.

Orbit around L_2	Impulsion to reach orbit($\Delta v_{\rm orb}$) ($\rm ms^{-1}$)	Max scan impulsion possible($\Delta v_{\rm prec}$) ($\rm ms^{-1}$)	Aspect angle of orbit ($\theta_{\rm orbit}$)	Max precession angle possible(α)
Large Lissajous	90	290	24°	38°
Medium Lissajous	267	113	12°	50°
Small Lissajous	332	48	6°	56°

there is a trade-off to be made with the fuel requirement that injection into the satellite orbit demands, as this leaves less fuel to drive the scan strategy. Table 3 shows the impulsion requirements to enter into three Lissajous orbits which we label as 'large', 'medium' and 'small'. We also show the remaining impulsion that would then be available to drive the scan assuming the satellite had a total impulsion of 380 $\rm ms^{-1}$ to use. Table 3 also shows the aspect angle of the satellite with respect to the Earth $\theta_{\rm orbit}$ and therefore, the maximum possible precession angle α.

The results of our systematic effect mitigation investigation are summarized in Fig. 7. In this figure, we have overplotted the constraints on the scan strategy due to the fuel and data transmission considerations discussed above. For each orbit (large, medium and small), we plot two lines which are represented by dotted, dashed and solid lines, respectively. The vertical line corresponds to the maximum precession angle for that orbit. The curved line is a line of constant impulsion which we must stay above. The result of this analysis shows that the best scan strategy for each orbit occurs at the limit of both constraints. The medium and small orbits allow much better scan strategies than the large orbit, with the medium orbit being slightly better than the small orbit.

Table 4. Parameters of the optimal scans at the different L_2 orbits (see Section 5 for details).

Scan	Boresight angle(β)	Precession (α)	Spin period ($T_{\rm spin}$) (s)	Precession period ($T_{\rm prec}$) (h)
Large Lissajous	57°	38°	166	15
Medium Lissajous	45°	50°	142	40
Medium Lissajous ($\beta = 50°$)	50°	50°	142	40
Small Lissajous	39°	56°	125	130

We show explicitly the optimal scan strategy of each orbit in Table 4. For the medium orbit, we suggest another option where we increase the boresight angle. In Figs 9 and 10, we plot the time integration and $|h_2|^2$ of the scan strategies presented in Table 4 for a range of mission lengths.

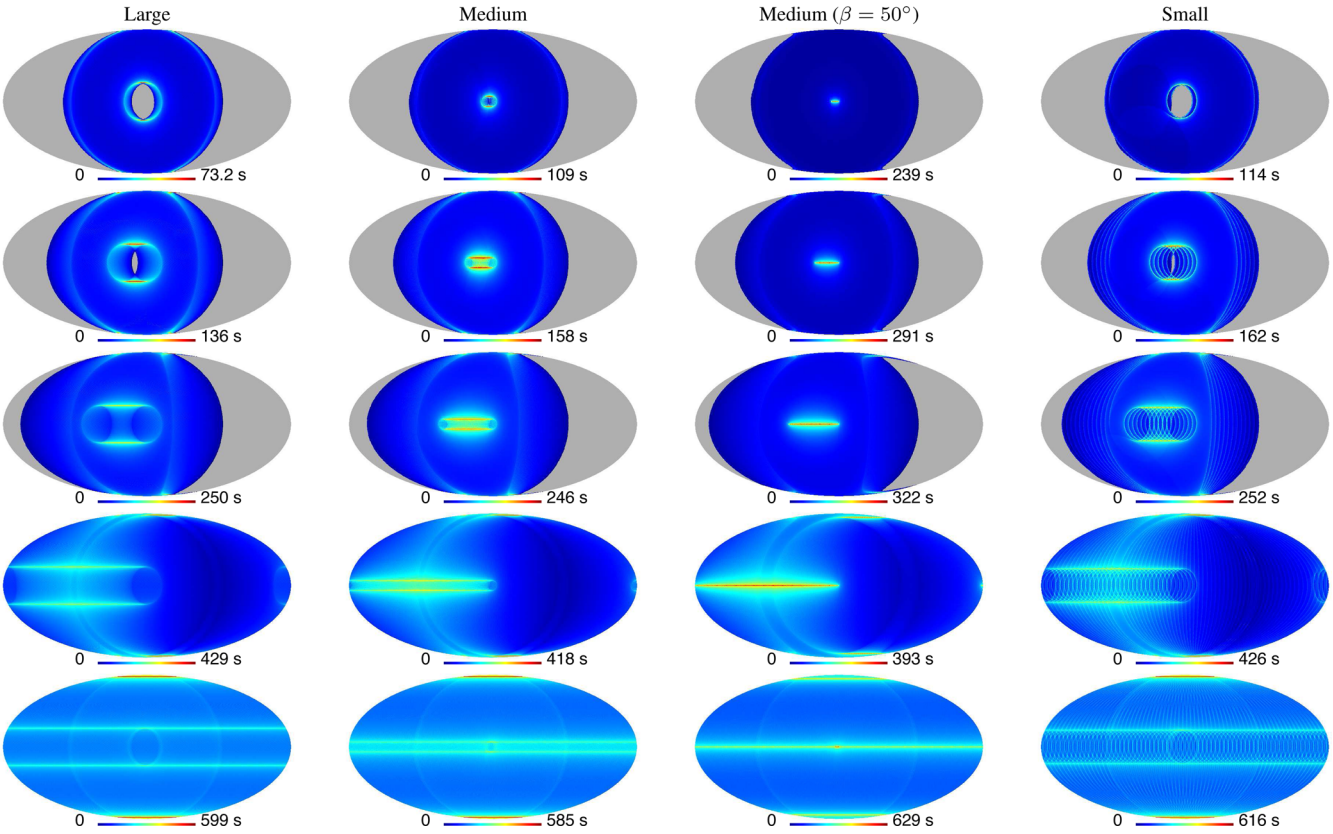

Figure 9. The time integration of each scan listed in Table 4 on a map of $N_{\rm side} = 128$. The rows correspond to the scan running for 10 d, 1 month, 2 months, 6 months and 1 yr, from top to bottom, respectively. All the plots are a Mollweide projection in Ecliptic coordinates.

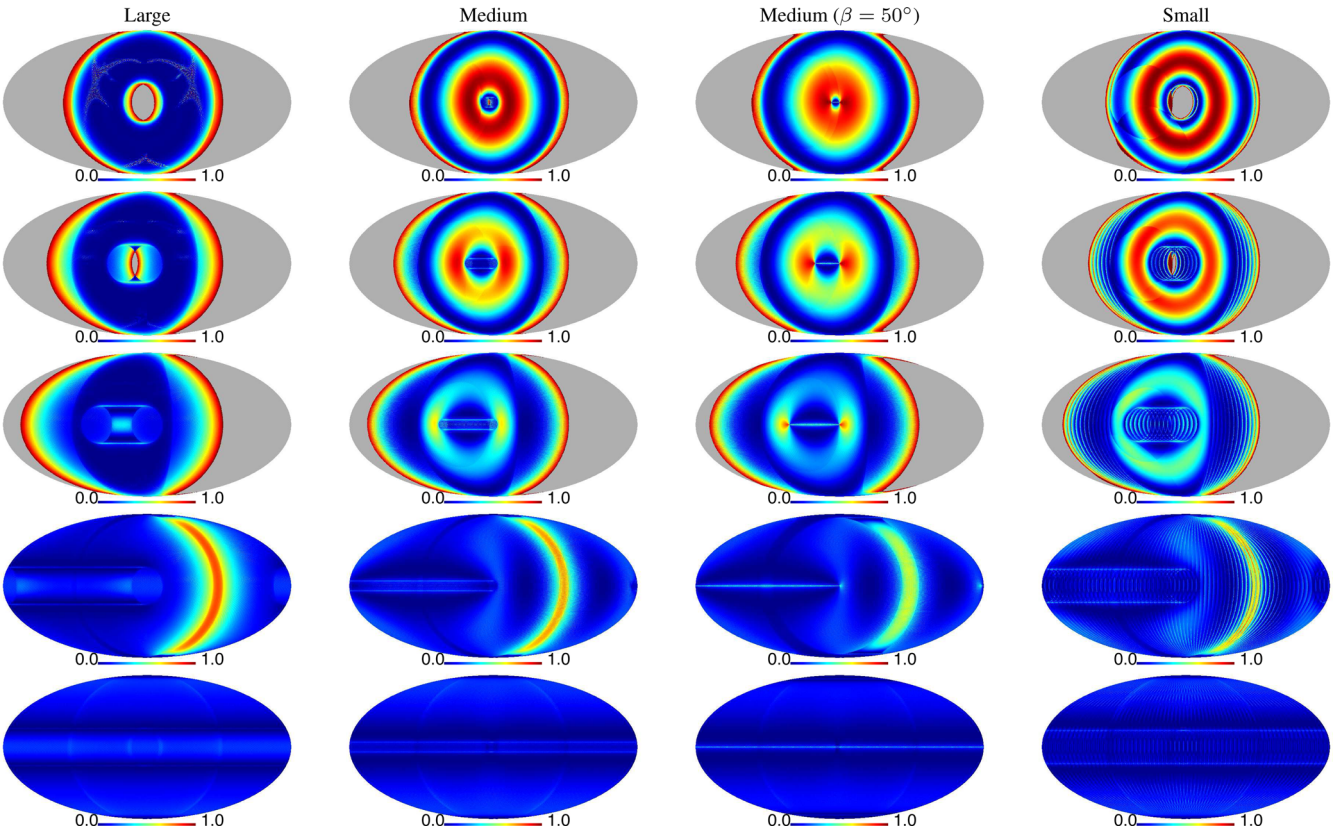

Figure 10. The value of $|h_2|^2$ of each scan listed in Table 4 on a map of $N_{\rm side} = 128$. As in Fig. 9, the rows correspond the scans running for 10 d, 1 month, 2 months, 6 months and 1 yr, from top to bottom, respectively. All the plots are a Mollweide projection in ecliptic coordinates.

Fig. 9 shows that all the scans can create a relatively even coverage over the sky after a year of scanning. It should be noted that in the 'small orbit' scenario we have too little fuel to drive a fast precession period. This slower precession has caused a less smooth time integration map. On shorter time-scales, the two 'medium orbit' scans can make half sky maps while the 'small orbit' and 'large orbit' scans require the Earth to orbit around the Sun to observe a full half-sky. The ability to make half-sky maps on short time-scales – of the order of tens of days – would be beneficial as this would allow time-dependent systematic effects to be investigated more easily. In Fig. 10, we plot the $|h_2|^2$ value of chosen scans. This shows how well the scans would allow us to make maps with single detectors. After a year, all scans have good polarization angle coverage and therefore single detector polarization maps will be possible. On shorter time-scales, however, this will not be possible. The orbit of the Earth around the sun is required to allow the telescope to observe large regions of the sky at many crossing angles. The second scan at the 'medium orbit' where we set the boresight angle $\beta = 50^\circ$ is intended to improve the polarization angle coverage on short time-scales. Fig. 10 does show a small improvement. The ability of the two 'medium orbits' to make half-sky maps on short time-scales, and to produce excellent polarization angle coverage over a year, make them both suitable choices for the COrE++ scan strategy.

6 DISCUSSION AND CONCLUSIONS

The CMB B-mode power spectrum is approximately four orders of magnitude fainter than the CMB temperature power spectrum. Any instrumental imperfections that couple temperature fluctuations to B-mode polarization must therefore be carefully controlled and/or removed. Here, we have investigated the role that a scan strategy can have in mitigating certain common systematics by averaging the error down with many crossing angles. In Section 2, we presented approximate analytical forms for the error on the recovered B-mode power spectrum that would result from differential gain, pointing and ellipticity if two detector pairs are used in a polarization experiment. By minimizing the h-values ($\tilde{h}_n$, see Table 1) of the scan strategy using multiple crossing angles, certain types of systematic effects can be averaged down. The different spins of the systematic effects mean that different h-values are relevant for mitigating different types of systematic effects.

By examining equations (26)–(28), we can see that since differential gain is a spin-0 systematic effect, it is suppressed by a factor $\langle|\tilde{h}_2|^2\rangle$, where the average is overall the pixels in the scan. Differential pointing is spin-1 and is therefore suppressed by factors involving $\langle|\tilde{h}_1|^2\rangle$ and $\langle|\tilde{h}_3|^2\rangle$. Differential ellipticity can couple temperature fluctuations to B-mode polarization in two ways: the first term in equation (28) is independent of the scan strategy and therefore if present, it will always result in spurious B-mode polarization regardless of the scan strategy. This has been shown a number of times before (O'Dea et al. 2007; Shimon et al. 2008; Wallis et al. 2014). If the orientation of the differential ellipticity is parallel or perpendicular to the polarization sensitivity direction, then the coupling from temperature will be of a pure E-mode form. Any misalignment there will be also be coupling to B-mode polarization. The second term of equation (28) models the effect due to a difference in the differential ellipticity between two pairs of detectors. This effect couples temperature fluctuations to both E and

B modes and can be mitigated with an appropriate scan strategy through the $\langle|\tilde{h}_4|^2\rangle$ term.

In Section 3, we used simulations to calculate the error on the B-mode power spectrum, shown in Fig. 3, for three example scan strategies. The larger precession angles and smaller boresight angles of the *WMAP* and EPIC scans reduce the even h-values and are therefore better at mitigating differential gain and differential ellipticity as compared to the *Planck* scan. The faster precession periods of the *WMAP* and EPIC scans reduce the odd h-values and are therefore better at mitigating differential pointing as well. In terms of future searches for inflationary B modes, our study suggests that differential gain is potentially the most problematic effect as it affects lower ℓ ranges.

Based on the validation by simulations in Section 3 as well as the pseudo-C_ℓ-based argument presented in Appendix A, we can be confident in using the analytic predictions for the error on the B-mode polarization power spectrum of Section 2. In Section 4, we combine the analytic analysis with a fast scan-strategy simulation code to search the scan-strategy parameter space for the optimal scan strategy, one which minimizes the error on the cosmological parameters. A key result is Fig. 6 where we have presented the $\langle|\tilde{h}_n|^2\rangle$ values for a range of satellite scan-strategy parameters.

Our main conclusions of the general investigation in Section 4 are as follows: (i) as long as $T_{\rm spin} \ll T_{\rm prec} \ll 1$ yr, the exact values of the time-scales are unimportant for mitigating systematics by multiple crossing angles. (ii) The main parameters of interest are the precession angle (α) and the boresight angle (β). By lowering β and increasing α, the scan strategy will make smaller circles on the sky. These small circles are beneficial for creating a wide range of orientation angles and are therefore effective in mitigating several of the systematic effects that we have considered. This is demonstrated in Fig. 7 where we plot the potential impact on the recovered value of the tensor-to-scalar ratio and lensing parameter $A_{\rm lens}^{\rm BB}$. For the particular levels of systematics that we have assumed, we find little difference in our preferred scan strategy regardless of whether we choose to target the inflationary B-mode signal on large angular scales or the lensing B-mode signal on smaller scales.

In Section 5, we consider these general observations and present the optimal scan strategies for three different Lissajous orbits. The different orbits require different amounts of fuel for injection, leaving different amounts to drive the scan. Also the different orbits allow different precessions angles due to constraints from the data transfer antenna (see Section 4.2). We chose the scans based on their ability to mitigate constant systematic errors in the cosmological parameters (see Fig. 7). Further to this, we require the scan to allow us to make maps of half the sky on short time-scales, in the order of tens of days. Fig. 9 shows that the two 'medium orbit' scans can make half-sky maps short time-scales, while the other two require the Earth to orbit around the Sun in order to observe half the sky.

During this optimization, we considered the practical constraints that limit the possible scan strategies. It should be noted that the constraint that limited our choice most is the constraint set by equation (40), where the precession angle is limited to ensure the antenna can transmit data to the earth. This forces us to limit the precession angle in the 'large orbit' to the point where half-maps cannot be made on short time-scales. The error on the cosmological parameters were also much worse for the 'large orbit' case than the other two because of the lower precession angle. If the antenna was designed to allow a larger aspect angle with respect to the Earth, then we could increase the precession angle. This would improve both these issues. As the precession period on the 'large orbit' is much faster, due to the increased amount of fuel, it would allow even faster half-sky maps, on the order of days instead of tens of days.

Ultimately, the choice of scan strategy for any future CMB polarization satellite mission will be a trade-off between these various competing scientific requirements, the instrumental capabilities and the fuel and data rate resources required. The results presented in this paper should prove useful for rapidly assessing the contribution of systematics mitigation in any such trade-off exercise for a future CMB polarization satellite.

ACKNOWLEDGEMENTS

The authors thank Clive Dickinson and Patrick Leahy for useful discussions and comments on the manuscript. We also acknowledge useful discussions with Pascal Rideau and Joel Michaud concerning practical constraints related to data transfer and to attitude and orbit control. CGRW acknowledges the award of an STFC quota studentship the support of the Engineering and Physical Sciences Research Council (grant no. EP/M011852/1). MLB acknowledges the European Research Council for support through the award of an ERC Starting Independent Researcher Grant (EC FP7 grant no. 280127). MLB also thanks the STFC for the award of Advanced and Halliday fellowships (grant no. ST/I005129/1). Some of the results in this paper have been derived using the HEALPIX (Górski et al. 2005) package.

REFERENCES

Bennett C. L. et al., 2003, ApJS, 148, 1
Bennett C. L. et al., 2013, ApJS, 208, 20
BICEP2 Collaboration et al., 2014, ApJ, 792, 62
BICEP2 Collaboration et al., 2015, ApJ, 814, 110
Bock J. et al., 2009, preprint (arXiv:0906.1188)
Brown M. L., Challinor A., North C. E., Johnson B. R., O'Dea D., Sutton D., 2009, MNRAS, 397, 634
Cantalupo C. M., Borrill J. D., Jaffe A. H., Kisner T. S., Stompor R., 2010, ApJS, 187, 212
Delabrouille J., 1998, A&AS, 127, 555
Delabrouille J., Gorski K. M., Hivon E., 1998, MNRAS, 298, 445
Delabrouille J., Puget J.-L., Lamarre J.-M., Gispert R., 2000, Astrophys. Lett. Commun., 37, 259
Dupac X., Tauber J., 2005, A&A, 430, 363
Feynman R., 1977, Lectures Notes in Physics, Vol. 1, The Feynman Lectures on Physics. California Institute of Technology, CA
Górski K. M., Hivon E., Banday A. J., Wandelt B. D., Hansen F. K., Reinecke M., Bartelmann M., 2005, ApJ, 622, 759
Hanson D. et al., 2013, Phys. Rev. Lett., 111, 141301
Hu W., Hedman M. M., Zaldarriaga M., 2003, Phys. Rev. D, 67, 043004
BICEP2 Collaborations Keck Array et al., 2015, Phys. Rev. Lett., 116, 031302
Kogut A. et al., 2011, J. Cosmol. Astropart. Phys., 7, 025
Leahy J. P. et al., 2010, A&A, 520, A8
Lewis A., Challinor A., 2011, CAMB: Code for Anisotropies in the Microwave Background, Astrophysics Source Code Library, ascl:1102.026
Markley F. L., Andrews S. F., O'Donnell J. R., Ward D. K., 2005, J. Guid. Control Dyn., 28, 385
Matsumura T. et al., 2014, J. Low Temp. Phys., 176, 733
O'Dea D., Challinor A., Johnson B. R., 2007, MNRAS, 376, 1767
Padin S. et al., 2008, Appl. Opt., 47, 4418
Planck Collaboration I, 2011, A&A, 536, A1
Planck Collaboration I, 2016, A&A, 594, A1
Planck Collaboration VII, 2016, A&A, 594, A7
Planck Collaboration VIII, 2016, A&A, 594, A8
Planck HFI Core Team et al., 2011, A&A, 536, A6

Shimon M., Keating B., Ponthieu N., Hivon E., 2008, Phys. Rev. D, 77, 083003
Sutton D. et al., 2010, MNRAS, 407, 1387
The COrE Collaboration et al., 2011, preprint (arXiv:1102.2181)
The Polarbear Collaboration: P. A. R. Ade et al., 2014, ApJ, 794, 171
Varshalovich D., Moskalev A., Khersonskii V., 1988, Quantum Theory of Angular Momentum., World Scientific Publishing Co. Inc., Singapore
Wallis C. G. R., Brown M. L., Battye R. A., Pisano G., Lamagna L., 2014, MNRAS, 442, 1963
Wallis C. G. R., Bonaldi A., Brown M. L., Battye R. A., 2015, preprint (arXiv:1503.03285)
Wu J. H. P. et al., 2007, ApJ, 665, 55

APPENDIX A: PSEUDO-C_ℓ APPROACH TO CALCULATING THE TEMPERATURE LEAKAGE

In Section 2, we have made an assumption about the way in which the scan strategy impacts on the leaked B-mode power spectrum. Specifically, we assumed that the effect of mitigation by the scan strategy can be approximated as a simple suppression of the leaked signal by the relevant $\langle|\tilde{h}_n|\rangle$ value (see Section 2) and that the direction of the leaked polarization would mean half of the power is of an E-mode form and the other half is of a B-mode form. This approximation allowed us to derive a relatively simple set of equations to describe the temperature to B-mode polarization power spectrum leakage. This simple set of equations was essential to quickly predict the leaked B-mode power spectrum for any given scan strategy as we did in Section 4. Here, we examine this approximation further and derive an exact analytical form for the leaked B-mode power spectrum for the case of differential gain. With this exact equation we can examine the approximation further.

We start from equation (20) which describes the leakage in the polarization map due to differential gain. We begin by defining the spherical harmonic modes of the CMB temperature field and of the differential gain as suppressed by the scan strategy:

$$\tilde{a}^T_{\ell m} = \int \mathrm{d}\Omega_0 Y^*_{\ell m}(\Omega) T^B(\Omega), \tag{A1}$$

$$H^{\pm 2}_{\ell m} = \int \mathrm{d}\Omega_{\pm 2} Y^*_{\ell m}(\Omega) \frac{1}{2}(\delta g_1 \pm \mathrm{i}\delta g_2)\tilde{h}_{\pm 2}(\Omega). \tag{A2}$$

We are interested in working out the error on the B-mode power spectrum. We therefore calculate the decomposition of the leaked polarization in terms of spin-weighted spherical harmonics,

$${}_2\tilde{a}_{\ell_1 m_1} = \int \mathrm{d}\Omega_2 Y^*_{\ell_1 m_1}(\Omega) \Delta P^{\mathrm{g}}(\Omega), \tag{A3}$$

$${}_{-2}\tilde{a}_{\ell_1 m_1} = \int \mathrm{d}\Omega_{-2} Y^*_{\ell_1 m_1}(\Omega) \Delta P^{\mathrm{g}*}(\Omega). \tag{A4}$$

Substituting these into our expression for ΔP^{g}, we find

$${}_{\pm 2}\tilde{a}_{\ell_1 m_1} = \int \mathrm{d}\Omega_{\pm 2} Y^*_{\ell_1 m_1}(\Omega) \frac{1}{2}(\delta g_1 \pm \mathrm{i}\delta g_2)\tilde{h}_{\pm 2}(\Omega) T^B(\Omega). \tag{A5}$$

We now substitute the spherical harmonic decomposition of the smoothed temperature field to find

$${}_{\pm 2}\tilde{a}_{\ell_1 m_1} = \int \mathrm{d}\Omega_{\pm 2} Y^*_{\ell_1 m_1}(\Omega) \frac{1}{2}(\delta g_1 \pm \mathrm{i}\delta g_2)\tilde{h}_{\pm 2}(\Omega) \times \sum_{\ell_2 m_2} \tilde{a}^T_{\ell_2 m_2}\, {}_0Y_{\ell_2 m_2}(\Omega) \tag{A6}$$

$$= \sum_{\ell_2 m_2} K^{\pm \ell_1 \ell_2}_{m_1 m_2} \tilde{a}^T_{\ell_2 m_2}, \tag{A7}$$

where we have defined the coupling kernel as

$$K^{\pm \ell_1 \ell_2}_{m_1 m_2} = \int \mathrm{d}\Omega_{\pm 2} Y^*_{\ell_1 m_1}(\Omega) \frac{1}{2}(\delta g_1 \pm \mathrm{i}\delta g_2)\tilde{h}_{\pm 2}(\Omega)\, {}_0Y_{\ell_2 m_2}(\Omega). \tag{A8}$$

We can now calculate the error on the recovered B-mode power spectrum. We start with the error on the measured B-mode power spectrum,

$$\Delta\tilde{C}^{\mathrm{BB}}_{\ell_1} = \frac{1}{2\ell_1 + 1} \sum_{m_1} \tilde{a}^B_{\ell_1 m_1} \tilde{a}^{B*}_{\ell_1 m_1} \tag{A9}$$

$$= \frac{1}{4(2\ell_1 + 1)} \sum_{m_1} \left(\tilde{a}^2_{\ell_1 m_1} - \tilde{a}^{-2}_{\ell_1 m_1}\right)\left(\tilde{a}^2_{\ell_1 m_1} - \tilde{a}^{-2}_{\ell_1 m_1}\right)^* \tag{A10}$$

$$= \frac{1}{4(2\ell_1 + 1)} \sum_{\substack{m_1 \\ \ell_2 m_2 \\ \ell'_2 m'_2}} \Big[K^{+^-\ell_1 \ell_2}_{m_1 m_2} \tilde{a}^T_{\ell_2 m_2} K^{+\ell_1 \ell'_2 *}_{m_1 m'_2} \tilde{a}^{T*}_{\ell'_2 m'_2} + K^{-\ell_1 \ell_2}_{m_1 m_2} \tilde{a}^T_{\ell_2 m_2} K^{-\ell_1 \ell'_2 *}_{m_1 m'_2} \tilde{a}^{T*}_{\ell'_2 m'_2} + (K^{+\ell_1 \ell_2}_{m_1 m_2} \tilde{a}^T_{\ell_2 m_2} K^{-\ell_1 \ell'_2 *}_{m_1 m'_2} \tilde{a}^{T*}_{\ell'_2 m'_2} + \mathrm{c.c.}) \Big], \tag{A11}$$

where the brackets denote the term to which the c.c. applies to. We can simplify this equation by requiring statistical isotropy of the CMB temperature field. This allows us to write $\tilde{a}^T_{\ell_1 m_1} \tilde{a}^{T*}_{\ell_2 m_2} = \delta_{\ell_1 \ell_2} \delta_{m_1 m_2} B^2_{\ell_1} \langle C^T_{\ell_1} \rangle$, where B_ℓ is the temperature beam window function and $\langle\rangle$ denotes averaging over CMB realizations. Substituting this result into equation (A11) and evaluating the Kronecker delta functions gives us

$$\langle \Delta\tilde{C}^{\mathrm{BB}}_{\ell_1} \rangle = \frac{1}{4(2\ell_1 + 1)} \sum_{\substack{m_1 \\ \ell_2 m_2}} \Big[K^{+\ell_1 \ell_2}_{m_1 m_2} K^{+\ell_1 \ell_2 *}_{m_1 m_2} + K^{-\ell_1 \ell_2}_{m_1 m_2} K^{-\ell_1 \ell_2 *}_{m_1 m_2} + (K^{+\ell_1 \ell_2}_{m_1 m_2} K^{-\ell_1 \ell_2 *}_{m_1 m_2} + \mathrm{c.c.}) \Big] B^2_{\ell_2} \langle C^{TT}_{\ell_2} \rangle \tag{A12}$$

$$= \sum_{\ell_2} M_{\ell_1 \ell_2} B^2_{\ell_2} \langle C^{TT}_{\ell_2} \rangle. \tag{A13}$$

To calculate the coupling operator we must first calculate a product of two coupling kernels. We do this in Appendix B. To calculate the error on the recovered B-mode power spectrum, we must then deconvolve for the polarization power spectrum. We assume that the temperature and polarization beam window functions are the same. This gives us

$$\langle \Delta C^{\mathrm{BB}}_{\ell_1} \rangle = \frac{1}{B^2_{\ell_1}} \sum_{\ell_2} M_{\ell_1 \ell_2} B^2_{\ell_2} \langle C^{TT}_{\ell_2} \rangle. \tag{A14}$$

As with all pseudo-C_ℓ coupling operators this matrix can be approximated by a diagonal matrix with values equal to the fraction of sky covered in the experiment. This approximation works best when the CMB power spectrum is close to constant. Here, the equivalent to the sky fraction is simply the average of the modulus squared of the window function $\frac{1}{2}(\delta g_1 + \mathrm{i}\delta g_2)\tilde{h}_2$. There is one difference in that half of the spurious polarization power will be in an E-mode form and the other half in a B-mode form. Therefore, we have

$$M_{\ell_1 \ell_2} \approx \frac{1}{8} |\delta g_1 + \mathrm{i}\delta g_2|^2 \langle |\tilde{h}_2|^2 \rangle \delta_{\ell_1 \ell_2}. \tag{A15}$$

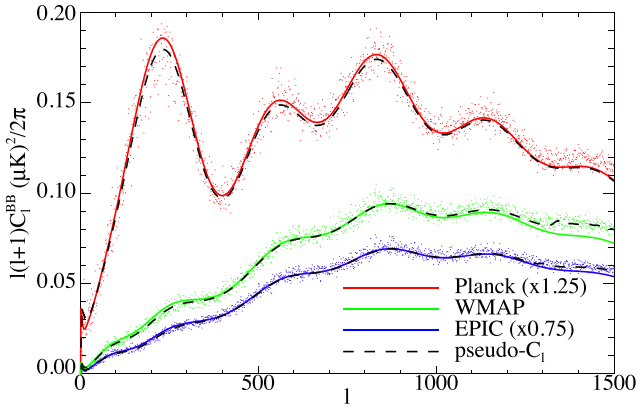

Figure A1. The recovered B-mode power spectrum when a differential gain systematic error is present assuming the *Planck*, *WMAP* and EPIC scan strategies (shown in red, green and blue, respectively). The points show the result for one simulation. The solid lines show the predictions for the recovered power spectrum using the approximate model of equation (26). The black dashed line shows the predictions using the full-coupling operator of equation (A14). There is good agreement between the two predictions for $\ell \lesssim 1000$. This provides strong justification for using the simple equations of Section 2 to predict the error on the B-mode power spectrum in Section 4. The small discrepancy between the pseudo-C_ℓ prediction and the simulation result for *Planck* at high ℓ is a numerical artefact associated with the simulation software.

With this approximation, equation (A14) reduces to equation (26). In Fig. A1, we show how well this approximation holds for realistic scan strategies. We plot the recovered B-mode power spectrum from simulations (as described in Section 3) assuming the *Planck*, *WMAP* and EPIC scan strategies, and including a differential gain systematic error in each detector pair. We also plot the predictions for the biased B-mode power:

$$C_\ell^{\mathrm{BB\,rec}} = C_\ell^{\mathrm{BB\,true}} + \Delta C_\ell^{\mathrm{BB}}. \tag{A16}$$

We plot two predictions for the biased power: one where the predicted error is of the simplified form of equation (26) and a second where the full-coupling operator of equation (A14) is used. The coupling-operator-based prediction is in excellent agreement with the simulations. However, it is also clear that the simplified formulae of Section 2 also provide an excellent approximation over the multipole range of interest.

APPENDIX B: PRODUCT OF TWO COUPLING KERNELS

In Appendix A, we use the product of two coupling kernels. Here we calculate this product. The definition of the coupling kernel gives us

$$K^{\pm\ell_1\ell_2}_{m_1m_2} = \int \mathrm{d}\Omega_{\pm2}Y^*_{\ell_1m_1}(\Omega)\frac{1}{2}(\delta g_1 \pm \mathrm{i}\delta g_2)\tilde{h}_{\pm2}(\Omega){}_0Y_{\ell_2m_2}(\Omega), \tag{B1}$$

$$= \sum_{\ell_3m_3} H^{\pm2}_{\ell_3m_3}\int \mathrm{d}\Omega_{\pm2}Y^*_{\ell_1m_1}(\Omega){}_0Y_{\ell_2m_2}(\Omega){}_{\pm2}Y_{\ell_2m_2}(\Omega), \tag{B2}$$

$$= \sum_{\ell_3m_3}(-1)^{m_1}H^{\pm2}_{\ell_3m_3}\sqrt{F_{\ell_1\ell_2\ell_3}} \times \begin{pmatrix} \ell_1 & \ell_2 & \ell_3 \\ -m_1 & m_2 & m_3 \end{pmatrix}\begin{pmatrix} \ell_1 & \ell_2 & \ell_3 \\ \mp2 & 0 & \pm2 \end{pmatrix}, \tag{B3}$$

where the second equality comes from an identity found in Varshalovich, Moskalev & Khersonskii (1988), and we have defined as

$$F_{\ell_1\ell_2\ell_3} = \frac{(2\ell_1+1)(2\ell_2+1)(2\ell_3+1)}{4\pi}. \tag{B4}$$

We are now in a position to calculate the product of two coupling kernels:

$$\sum_{m_1m_2} K^{\pm\ell_1\ell_2}_{m_1m_2}K^{\pm\ell_1\ell_2*}_{m_1m_2} = \sum_{\substack{m_1m_2\\ \ell_3m_3\\ \ell_3'm_3'}} H^{\pm2}_{\ell_3m_3}H^{\pm2*}_{\ell_3'm_3'}\sqrt{F_{\ell_1\ell_2\ell_3}} \times \begin{pmatrix} \ell_1 & \ell_2 & \ell_3 \\ -m_1 & m_2 & m_3 \end{pmatrix}\begin{pmatrix} \ell_1 & \ell_2 & \ell_3 \\ \mp2 & 0 & \pm2 \end{pmatrix} \times \sqrt{F_{\ell_1\ell_2\ell_3'}}\begin{pmatrix} \ell_1 & \ell_2 & \ell_3' \\ -m_1 & m_2 & m_3' \end{pmatrix} \times \begin{pmatrix} \ell_1 & \ell_2 & \ell_3' \\ \mp2 & 0 & \pm2 \end{pmatrix}. \tag{B5}$$

To simplify this result, we use the orthogonality relation,

$$\sum_{m_1m_2}\begin{pmatrix} \ell_1 & \ell_2 & \ell_3 \\ m_1 & m_2 & m_3 \end{pmatrix}\begin{pmatrix} \ell_1 & \ell_2 & \ell_3' \\ m_1 & m_2 & m_3' \end{pmatrix} = \frac{1}{2\ell_3+1}\delta_{\ell_3,\ell_3'}\delta_{m_3,m_3'}. \tag{B6}$$

Evaluating the Kronecker delta function leads to

$$\sum_{m_1m_2} K^{\pm\ell_1\ell_2}_{m_1m_2}K^{\pm\ell_1\ell_2*}_{m_1m_2} = \sum_{\ell_3} F_{\ell_1\ell_2\ell_3}\mathcal{H}^{\pm\pm}_{\ell_3} \times \begin{pmatrix} \ell_1 & \ell_2 & \ell_3 \\ \mp2 & 0 & \pm2 \end{pmatrix}\begin{pmatrix} \ell_1 & \ell_2 & \ell_3 \\ \mp2 & 0 & \pm2 \end{pmatrix}, \tag{B7}$$

where we have defined the spin power spectrum of the window function as

$$\mathcal{H}^{\pm\pm}_{\ell_3} = \frac{1}{2\ell_3+1}\sum_{m_3}H^{\pm2}_{\ell_3m_3}H^{\pm2*}_{\ell_3m_3}. \tag{B8}$$

This paper has been typeset from a TEX/LATEX file prepared by the author.